

An XMM-Newton spectral survey of 12 micron selected galaxies. I. X-ray data

Murray Brightman^{2,1*} and Kirpal Nandra^{2,1}

¹*Astrophysics Group, Imperial College London, Blackett Laboratory, Prince Consort Road, London SW7 2AW*

²*Max-Planck-Institut für extraterrestrische Physik, Giessenbachstrasse 1, D-85748, Garching bei München, Germany*

Accepted 0000 December 00. Received 0000 December 00; in original form 0000 October 00

ABSTRACT

We present an X-ray spectral analysis of 126 galaxies of the 12 micron galaxy sample (12MGS). By studying this sample at X-ray wavelengths, we aim to determine the intrinsic power, continuum shape and obscuration level in these sources. We improve upon previous works by the use of superior data in the form of higher signal to noise spectra, finer spectral resolution and a broader band pass from *XMM-Newton*. We pay particular attention to Compton thick AGN with the help of new spectral fitting models that we have produced, which are based on Monte-Carlo simulations of X-ray radiative transfer, using both a spherical and torus geometry, and taking into account Compton scattering and iron fluorescence. We use this data to show that with a torus geometry, unobscured sight lines can achieve a maximum equivalent width (EW) of the Fe $K\alpha$ line of ~ 150 eV, originally shown by Ghisellini, Haardt & Matt (1994). In order for this to be exceeded, the line of sight must be obscured with $N_{\text{H}} > 10^{23}$ cm $^{-2}$, as we show for one case, NGC 3690. We also calculate flux suppression factors from the simulated data, the main conclusion from which is that for $N_{\text{H}} \geq 10^{25}$ cm $^{-2}$, the X-ray flux is suppressed by a factor of at least 10 in all X-ray bands and at all redshifts, revealing the biases present against these extremely heavily obscured systems inherent in all X-ray surveys. Furthermore, we confirm previous results from Murphy & Yaqoob (2009) that show that the reflection fraction determined from slab geometries is underestimated with respect to toroidal geometries. For the 12 micron selected galaxies, we investigate the distribution of X-ray power-law indices, finding that the mean ($\langle \Gamma \rangle = 1.90_{-0.07}^{+0.05}$ and $\sigma_{\Gamma} = 0.31_{-0.05}^{+0.05}$) is consistent with previous works, and that the distribution of Γ for obscured and unobscured sources is consistent with the source populations being the same, in general support of unification schemes. We determine a Compton thick fraction for the X-ray AGN in our sample to be $18 \pm 5\%$ which is higher than the hard X-ray (> 10 keV) selected samples. Finally we find that the obscured fraction for our sample is a strong function of X-ray luminosity, peaking at a luminosity of $\sim 10^{42-43}$ erg s $^{-1}$.

Key words: galaxies: active - galaxies: Seyfert - X-rays: galaxies

1 INTRODUCTION

Studying AGN at X-ray wavelengths allows an assessment of the intrinsic source properties, such as the measurement of the continuum and the source power, due to the ability of X-rays to penetrate and measure large columns of obscuring material. This makes X-ray observations essential for testing AGN unification schemes (Awaki et al. 1991) which invoke obscuration to explain the perceived difference between

Seyfert 1s and Seyfert 2s (Antonucci 1993; Urry & Padovani 1995). The N_{H} and Γ distributions for AGN are also an important ingredients for synthesis models of the cosmic X-ray background (XRB, Gilli, Comastri & Hasinger 2007).

Most of our knowledge of the X-ray properties of local AGN comes from X-ray selected samples, such as the Piccinotti et al. (1982) sample derived from *HEAO 1* observations (e.g. Turner & Pounds 1989; Nandra & Pounds 1994). X-ray selection of AGN is in principle very effective as in this band the nucleus predominantly outshines the host galaxy, and can penetrate obscuration. The hard X-

* E-mail: mbright@mpe.mpg.de

ray telescopes aboard *INTEGRAL* and *Swift* and their large sky coverage have allowed for the compilation of hard X-ray selected AGN catalogues. Beckmann et al. (2006) and Beckmann et al. (2009) have presented catalogues for *INTEGRAL* selected AGN, which total 199 after 5 years of observations, and Tueller et al. (2008) and Tueller et al. (2010) have presented 229 *Swift/BAT* selected Seyfert galaxies after 22 months of observations. However, the discovery from these surveys seems to be that the fraction of Compton thick AGN detected is smaller than expected from XRB studies (Gilli, Comastri & Hasinger 2007). This points to the empirical fact that even the X-ray band is biased against the most obscured, Compton thick, AGN. X-ray selection at energies greater than 10 keV is less affected by Compton thick obscuration than 2-10 keV selection though.

An alternative to X-ray AGN selection is mid-infrared (MIR) selection where the primary radiation of the AGN is re-emitted after having been reprocessed by hot dust. The extended *IRAS* 12 micron galaxy sample (12MGS - Rush, Malkan & Spinoglio 1993, RMS) is a sample of 893 MIR selected local galaxies which contains a high fraction of AGN (13% at the time of publication, RMS). The sample is taken from the *IRAS Faint Source Catalogue, version 2 (FSC-2)* and imposes a flux limit of 0.22 Jy, including only sources with a rising flux density from 12 to 60 microns (to exclude stars) and with a galactic latitude of $|b| \geq 25$ deg. Being selected in the mid-infrared (MIR) this sample is also relatively unbiased against absorption, low luminosity systems and ‘hidden AGN’. Spinoglio & Malkan (1989) showed that a wide variety of AGN types emit a constant fraction of their bolometric luminosities at this wavelength, and furthermore shown to be true for star forming galaxies as well by Spinoglio et al. (1995). The 12MGS should be therefore also representative of the true number of different active galaxy types in relation to each other.

It is possible, though, that even at 12 μm , the AGN emission may be suppressed in the most heavily obscured nuclei. Pier & Krolik (1992) present radiative transfer modelling for the infrared emission from dust tori for varying torus orientations. The most significant result of this study was that throughout the infrared, the emission in the edge-on direction is weaker with respect to the face-on direction, and at 12 μm , the difference can be up to several orders of magnitude for optically thick tori. These models suggest that AGN selection at 12 microns is biased against heavily obscured nuclei. However, recently this was tested observationally by Horst et al. (2008). They used high resolution 12.3 μm imaging of a sample of local Seyfert nuclei, with X-ray data to explore the ratio of the MIR to intrinsic X-ray nuclear luminosities in order to detect any difference between the obscured nuclei (Seyfert 2s) and unobscured nuclei (Seyfert 1s). As the X-ray luminosities have been corrected for absorption, L_X should represent the intrinsic emission from the nucleus. For smooth tori modelled by Pier & Krolik (1992), obscured systems should then present lower L_{MIR}/L_X ratios than unobscured systems due to the suppressed MIR flux seen in these systems. A difference of an order of magnitude for a difference in N_H of between $\sim 10^{20}$ and $\sim 10^{24}$ cm^{-2} is predicted by the torus models, and should be measurable. However, this is not seen observationally, as Horst et al. (2008) find no significant difference between Seyfert 1s and Seyfert 2s, or even Compton

thick nuclei. They argue from this that the torus may not be smooth, and instead clumpy, where the torus is seen to be optically thin, but the clumps are optically thick, though with a small volume filling factor. Most importantly for this work though, it suggests that 12 micron selection is in fact not heavily biased against obscuration. This therefore makes the 12MGS the ideal parent sample for study of obscuration and unification using X-ray observations and is as such the subject of this paper.

The 12MGS has previously been studied at X-ray wavelengths by Barcons et al. (1995) who used hard X-ray observations by *HEAO 1*, and at soft X-rays by Rush et al. (1996) with *ROSAT* data. Barcons et al. (1995) use the X-ray and IR data sets to show that most of the local X-ray emissivity originates from Seyfert galaxies and that most of the local 2-10 keV X-ray luminosity function between 10^{42} and 10^{46} erg s^{-1} can be accounted for by 12 micron emitting AGN. They also test the unification scheme and come to the conclusion that it must be modified to include the reduction of the covering fraction of the torus with increasing source luminosity, an observation first suggested by Lawrence (1991) which has come to be known as the ‘receding torus model’. Rush et al. (1996) conducted a spectral analysis of the 0.1-2.4 keV *ROSAT* data. For spectra with enough counts, they fit absorbed power-laws, finding a median soft X-ray spectral index of 2.3 for all Seyfert types.

In this paper, we present an X-ray spectral analysis of the galaxies of the 12MGS with an observation by *XMM-Newton*, which consists of a heterogeneous mix of Seyferts, LINERs and star-forming galaxies. We focus on the X-ray spectral properties of the sources without regard for their optical spectroscopic types and use X-ray luminosity to select unambiguous AGN. In a companion paper though, we continue our investigation into this sample combining the X-ray data from this paper with optical spectroscopic and infrared data. In Section 2 we present work on Monte-Carlo simulations of X-ray radiative transport which we use in our spectral analysis. Section 3 describes our spectral fitting methods and Section 4 gives our spectral fitting results. Finally we discuss all of these results in Section 5 and present our conclusions in Section 6.

2 NEW X-RAY SPECTRAL MODELS FOR HEAVILY OBSCURED SOURCES

In our X-ray spectral analysis of the 12MGS, we pay particular attention to whether sources are Compton thick, as the Compton thick fraction is particularly crucial for the XRB models and knowledge of the accretion history of the universe. Compton thick AGN are most commonly identified in the 2-10 keV X-ray band by the measurement of a flat spectrum, where $\Gamma < 1.0$, and the equivalent width (EW) of the iron $K\alpha$ line has been measured to be high (EW > 1 keV, Matt et al. 1996). This is typical of a reflection spectrum, produced by X-ray scattering from an optically thick surface, such as the accretion disk or wall of the torus in AGN. It is indicative of heavy obscuration of the central source as the reflection is dominating over the transmission of the intrinsic power-law through the obscuring material.

In some cases, the transmission of the intrinsic power-law can be detected in the 2-10 keV band for these heavily

obscured sources. However, due to the extreme suppression of flux in this band at these high column densities, this is very difficult. Also at the high optical depths in these Compton thick sources the calculations for modelling the transmission spectrum become non-linear due to multiple scatterings. Thus, models describing simple attenuation of the spectrum by absorption and scattering become invalid.

Therefore, accurate models that correctly account for Compton scattering, especially multiple scatterings, are necessary when fitting the spectra of these sources. Currently, the best established model within XSPEC for correctly describing X-ray reprocessing by photoelectric absorption and Compton scattering is `plcabs`. This model describes the X-ray transmission from an isotropic source at the centre of a uniform spherical distribution of matter. It is valid up to energies between 10 and 18.5 keV and up to column densities of $5 \times 10^{24} \text{ cm}^{-2}$ (Yaqoob 1997). Unfortunately `plcabs` has a limited range of validity and does not include line emission, modelling the continuum only. Recently, two works by Ikeda et al. (2009) and Murphy & Yaqoob (2009) have produced improved Monte-Carlo models based on a toroidal obscuring medium similar to calculations by Ghisellini et al. (1994) which include iron line emission.

Here we have carried out our own Monte-Carlo simulations based mainly on the methods of Nandra & George (1994, NG94), but with a point-source of X-rays located at the centre of both a spherical and toroidal distribution of gas emitting a power-law spectrum. These simulations follow the propagation of X-ray photons which interact with the medium via Compton scattering or photo-electric absorption, which can then result in fluorescent emission. The type of interaction is determined by the energy dependent interaction cross sections. We calculate the Compton scattering cross section described in Rybicki & Lightman (1986) and calculate the photo-electric absorption cross sections using data from Verner et al. (1996), using abundances from Anders & Grevesse (1989) and fluorescent yields from Bambynek et al. (1972). The medium is assumed to be of constant density and there is no dependence of the line of sight column density on the inclination angle of the observer, with the exception of the unobscured sight lines in the torus geometry which have a zero column density. Fig. 1 illustrates the geometry used in the torus simulations, where the shading only serves to differentiate the different opening angles used, and does not correspond to density.

The models importantly also include line emission, most significantly iron $K\alpha$ (6.4 keV), but also iron $K\beta$ (7.06 keV) and $K\alpha$ emission from several other elements described in Table 1. As mentioned before, the EW of the iron line is strongly dependent on absorption, as is the shape of the line's Compton shoulder. The Compton shoulder feature is seen on the red side of the line, and is a result of Compton down scattering of the first order line and depends on the scattering optical depth. In these models, the flux of the line and its spectral shape are inextricably linked to N_H and therefore it provides additional constraints on this parameter when spectral fitting. Yaqoob & Murphy (2010) present a detailed examination of the Compton shoulder's properties, showing that it is also dependent on spectral shape and geometry of the absorber, and hence contains valuable information given that it is well resolved.

We have made several improvements on the previous

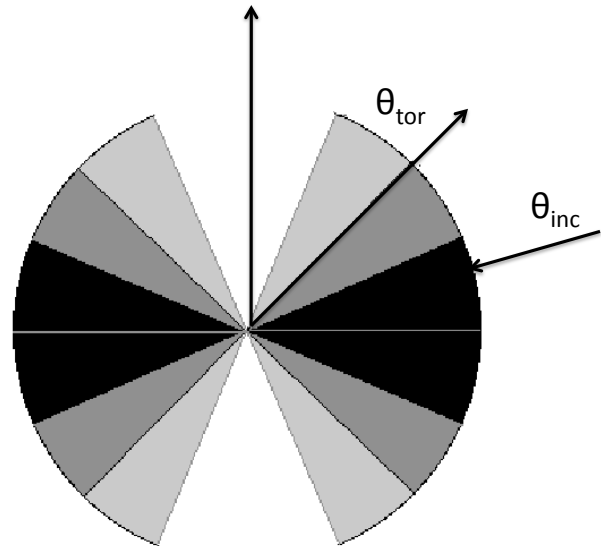


Figure 1. Geometry of the biconical torus distribution of matter used. The shading only serves to differentiate the different opening angles used, and does not correspond to density.

work by NG94, many with the aim to improve computational times and spectral quality. These include the use of a technique described by Lucy (2002), in which radiation in Monte-Carlo simulations is represented by indivisible monochromatic ‘packets’ of energy which propagate through the system in the same way as the photons were simulated previously. This technique allowed us to inject any number of quanta at each energy without sacrificing the power-law relation. Each packet is assigned a ‘weight’ dependent on the width of the energy bin from which it is injected, the number of packets being injected at that energy and the energy-flux relation taken from the power-law.

$$weight = \frac{\Delta E \times F(E)}{N_{packets}}$$

The weights of the emergent packets are then binned at the end in the same way. This technique has the advantage that it is possible to vary the number of quanta released depending on how detailed the spectrum needs to be at that energy. It is especially useful for increasing the signal to noise of the output spectrum around the iron K-shell regime (6-8 keV). Valuable computational time may also be saved by decreasing the signal to noise in the featureless parts of the spectrum, above 10 keV for example. We also made an improvement to the original method by introducing variable elemental abundances (with respect to the abundance of Hydrogen). The abundance of iron is a separate parameter also, as the modelling of the iron lines are particularly sensitive to this.

We have constructed table models for use within XSPEC, which we call `trans` for the spherical distribution of matter, and `torus` for the toroidal distribution of matter. The parameters of the models are the line of sight column density of the neutral material ($10^{20} \text{ cm}^{-2} \leq N_H \leq 10^{26} \text{ cm}^{-2}$) and the photon index of the intrinsic power-law ($1 \leq \Gamma \leq 3$). For `trans` the abundance of iron ($0.1 \text{ solar} \leq Fe_{abund} \leq 10 \text{ so-$

Element	Abundance w.r.t Hydrogen ($\times 10^{-4}$)	Line energy (keV)	Edge energy (keV)	Fluorescent yield, Y
Carbon	3.63	0.28	0.29	0.0025
Oxygen	8.51	0.53	0.54	0.0086
Neon	1.23	0.85	0.87	0.0183
Magnesium	0.38	1.25	1.31	0.0303
Silicon	0.355	1.74	1.85	0.043
Argon	0.0363	2.96	3.20	0.122
Calcium	0.0229	3.69	4.04	0.168
Chromium	0.00484	5.41	6.00	0.283
Iron	0.468	6.40, 7.06	7.12	0.342
Nickel	0.0178	7.48	8.35	0.432

Table 1. Elemental data used in the Monte-Carlo simulations. Abundances are from Anders & Grevesse (1989), and fluorescent yields are from Bambynek et al. (1972)

lar) and the total elemental abundance ($0.1 \text{ solar} \leq \text{abund.} \leq 10 \text{ solar}$) are included as parameters, whereas for **torus**, the opening angle of the torus ($25.8^\circ \leq \theta_{\text{tor}} \leq 84.3^\circ$) and the inclination angle of the torus ($18.2^\circ \leq \theta_i \leq 87.1^\circ$) are included. Both models have validity in an energy range of 0.1 keV to 320 keV.

2.0.1 Fe K α Line Equivalent Width Calculations

We also use the results from our Monte-Carlo simulations to make predictions of the equivalent width of the iron K α line for both geometries given a set of model parameters. In the simulations the photon packets produced by a simulated iron K-shell fluorescence are flagged and summed as they exit the simulation. In this way, we can calculate the equivalent width of the line produced, by the sum of iron K α photon flux divided by the continuum level at 6.4 keV and the width of the energy bin at this energy. The calculation represents the EW of the entire line, including the Compton shoulder.

Figure 2 shows how the EW varies with N_{H} , Γ and the iron and elemental abundances for the spherical geometry. The EW of the line increases linearly versus N_{H} up to $\tau \sim 0.1$, where the relationship increases faster than linearly beyond that. This is due to the suppression of the continuum at 6.4 keV at high column densities, against which the EW is measured, but possibly also due to the greater number of photons at and above the 7.1 keV iron K shell threshold having been down-scattered from higher energies. Increasing the iron abundance will as expected increase the EW of the line due to the greater number of iron atoms per hydrogen atom to produce the transition. The abundance of the other elements also effects the EW of the iron line, though not as significantly. The EW is seen to increase from low elemental abundance to $\sim 0.3 \times$ solar abundance. This is also expected as an increase in the elemental abundances will cause some continuum suppression at 6.4 keV, leading to an increase in the EW of the iron line. This trend flattens off for $N_{\text{H}} < 10^{23}$ as the elemental abundance increases beyond solar though, but for higher N_{H} values, the EW decreases above $\sim 0.3 \times$ solar abundance. Again though, at these extreme N_{H} values the continuum against which the EW is measured is very suppressed so it is difficult to know if this behaviour is real. Figure 3 shows how the EW of the iron line changes with

N_{H} in the torus model for different torus parameters. The left plot shows this relationship for equatorial sight-lines, where the different lines show different opening angles. The smaller the opening angle, and hence the larger solid angle of the torus, the larger the EW of the iron line. The EW reaches a maximum here of 4 keV, 2.1 keV and 1.6 keV for torus opening angles of $\theta_{\text{tor}} = 30^\circ$, 60° and 75° . The middle panel shows the same relationship, but for the polar sight-line. The EWs here are systematically lower due to the greater, unabsorbed continuum. The EWs reach a maximum of 150 eV, 96 eV and 63 eV for 30° , 60° and 75° opening angles. Due to this dependence on column density and the opening angle of the torus, it may be possible to make inferences about the circum-nuclear matter distribution in AGN from the EW of the iron line, even for unobscured sources. For example, unobscured sources with an EW greater than ~ 150 eV must have a very narrow opening in the torus, or else super-solar iron abundance. Alternatively, the source may not be unobscured at all. It may be very heavily obscured with the intrinsic emission extremely suppressed below 10 keV, and only a weak scattered or galactic component visible. We use these data later when determining the Compton thick nature of our sources. Finally the right panel in this figure shows the variation of EW for a fixed torus opening angle of 60° , and varying viewing angles, and shows that for unobscured sources, the viewing angle does not affect the EW of the iron line greatly.

2.0.2 X-ray flux suppression

We also use the results from our new models to calculate expected flux suppression factors for different X-ray bands, as a function of absorption and for different redshifts. This information is useful when estimating the N_{H} , given only an observed flux and a predicted intrinsic flux, or when considering the biases against heavily obscured sources in X-ray selected AGN samples. We do this for both spherical and toroidal distributions of matter with solar abundances, $\Gamma = 2$ intrinsic power-laws and for the case of the torus, a 60° opening angle and 90° viewing angle. Figure 4 gives the flux suppression factor at different column densities and in different bands. The flux suppression factor is calculated as

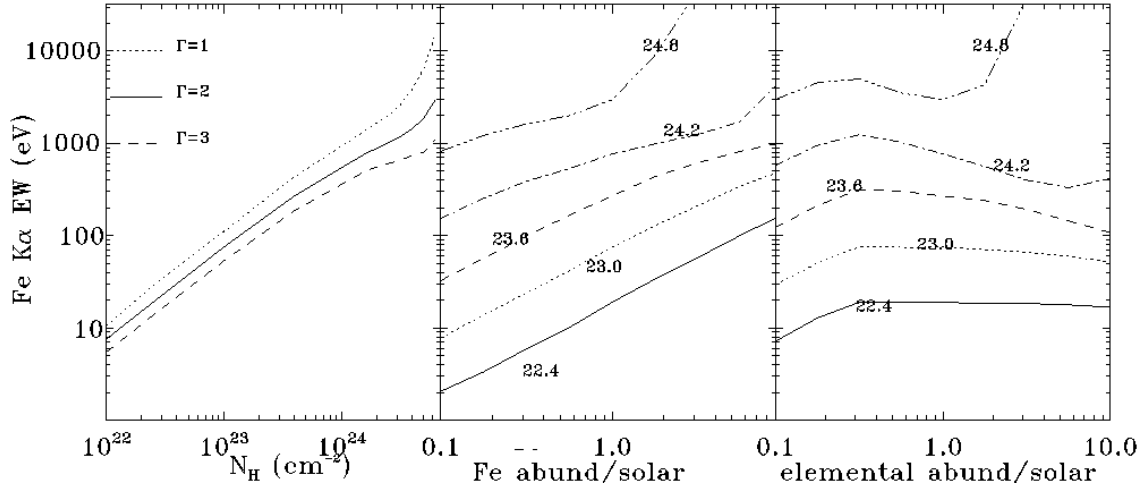


Figure 2. Predictions of the equivalent width of the iron K α line for the spherical distribution and varying parameters. Left panel - EW vs N_{H} with the three lines representing $\Gamma = 1, 2$ and 3 in ascending order for solar abundances. Middle panel - EW vs iron abundance (in units of solar abundance) with different lines for varying N_{H} labelled in the figure as $\log_{10}(N_{\text{H}}/\text{cm}^{-2})$ and fixed $\Gamma=2$. Right panel EW vs total elemental abundance (in units of solar abundance) with different lines for varying N_{H} labelled in the figure as $\log_{10}(N_{\text{H}}/\text{cm}^{-2})$ and fixed $\Gamma=2$.

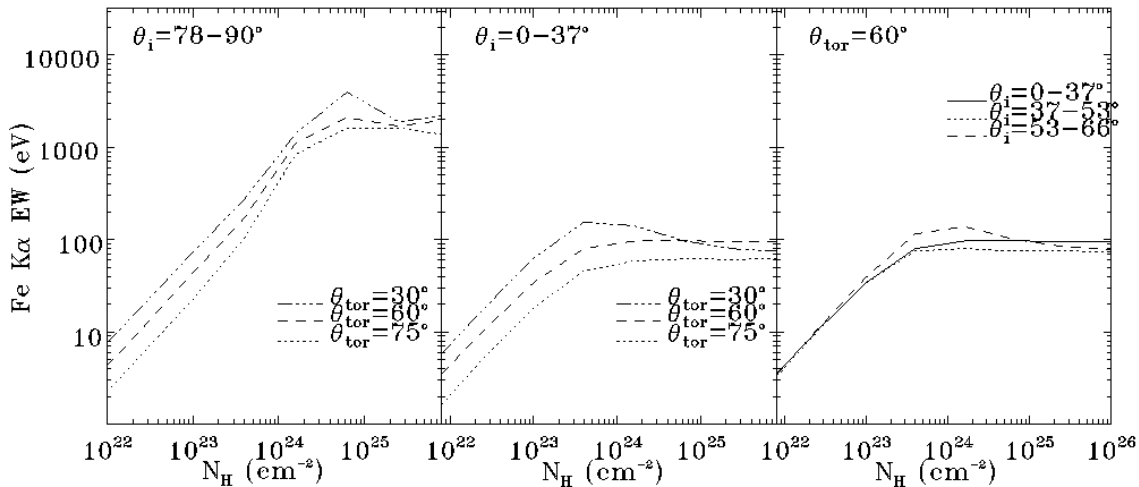


Figure 3. Predictions of the equivalent width of the iron K α line for the torus distribution with varying torus opening angles and viewing angles. Left panel - EW vs N_{H} for equatorial viewing angles ($78-90^\circ$), and varying torus opening angles, θ_{tor} . Middle panel - EW vs N_{H} for polar viewing angles ($0-37^\circ$), and varying torus opening angles, θ_{tor} ; Right panel - EW vs N_{H} for different viewing angles, θ_i , with a fixed torus opening angle, $\theta_{\text{tor}}=60^\circ$; All with fixed $\Gamma=2$.

the intrinsic, unabsorbed energy flux in a particular band divided by the flux observed in that band.

The attenuation of the intrinsic emission by the absorbing material is evident as the N_{H} increases. For the spherical case, at a redshift of zero and for energy bands above 10 keV, the effect of this attenuation is negligible (< 2) for N_{H} up to $\sim 4 \times 10^{24} \text{ cm}^{-2}$, however, at $N_{\text{H}}=10^{25} \text{ cm}^{-2}$, the flux in these bands is suppressed by a factor of 10. This relationship is roughly independent of redshift for these bands. For the 2-10 keV band, locally, the flux is suppressed by a factor of 10 at $N_{\text{H}}=6 \times 10^{23} \text{ cm}^{-2}$. As redshift increases, the N_{H} at which the flux suppression factor reaches 10 increases due to the photo-electric absorption cut-off being redshifted

through the band. The N_{H} at which the flux suppression factor is 10 for redshifts one, two and three is 3×10^{24} , 7×10^{24} and 10^{25} cm^{-2} respectively for the 2-10 keV band.

Flux suppression factors calculated from the torus geometry behave similarly to the spherical case until $\sim 4 \times 10^{24} \text{ cm}^{-2}$ where they flatten off, rather than continuing to increase as they do for the spherical geometry. This is due to reflected X-ray flux from the torus which is present regardless of the level of obscuration seen directly through the torus. The flux suppression factor flattens off at ~ 100 for the 2-10 keV band at $z=0$, however, this improves to ~ 30 , ~ 15 and ~ 12 for $z=1, 2$ and 3 due to this band observing higher energy rest-frame X-rays which are less effected

by photo-electric absorption that dominate in the 2-10 keV band at rest-frame energies. For the > 10 keV bands, the flux suppression factor levels off at ~ 10 at all redshifts. At $z=3$, flux suppression in the 2-10 keV band is less than that seen in the 20-100 keV (INTEGRAL) and 14-195 keV (Swift/BAT) bands. This is most likely due to the Compton hump, produced by the 'down-scattering' of higher energy X-rays and peaks at rest-frame ~ 30 keV. At $z=3$ it appears directly in the 2-10 keV band, whereas the higher energy bands only view the tail of the hump.

For both geometries, all redshifts and X-ray bands, flux suppression is > 10 at $N_{\text{H}}=10^{25}\text{cm}^{-2}$. This shows that for sources with extreme obscuration, even X-rays are strongly attenuated.

3 X-RAY SPECTRAL ANALYSIS

The X-ray spectra of galaxies and AGN are very complicated and as such it is necessary to utilise high signal to noise spectra with good spectral resolution and a wide band pass in order to correctly determine the source properties. These have been provided by *XMM-Newton* better than ever before, so in using data obtained from this observatory, we aim to gain new and improved insights into the X-ray spectral properties of the 12MGS. Rush et al. (1996) studied the soft X-ray spectra of the 12MGS from *ROSAT* All-sky survey observations, but in doing so will have missed any moderate to heavily obscured emission, and furthermore, the signal to noise and resolution of *ROSAT* was incomparable to that of *XMM-Newton*. Barcons et al. (1995) used hard X-ray data from *HEAO 1* and will therefore have been sensitive to obscured sources. However, their data also suffered from poor signal to noise and low spectral resolution, meaning they could only determine the source intensity with no meaningful investigation of the absorption or continuum slope.

We develop a systematic approach to the spectral fitting of our sample in order to determine the intrinsic X-ray continuum slope, Γ , the neutral absorption column density, N_{H} , and the 2-10 keV intrinsic source power, L_{X} . Characterising Γ is necessary for insights into the primary X-ray generation process in AGN, thought to be the Comptonisation of accretion disk photons by a hot corona (Sunyaev & Titarchuk 1980; Haardt & Maraschi 1991). This intrinsic source continuum parameter is also useful for comparing different source populations, such as Seyfert 1s and 2s, to determine if their central engines are the same, as predicted by unified schemes. Determining the N_{H} distribution in AGN is a key ingredient to XRB synthesis models, and measuring the intrinsic power allows for comparison to the power at other wavelengths. We will discuss most of these issues in a subsequent publication however, and we focus on an accurate determination of these parameters here.

3.1 Sample selection and data reduction

The sample of observations presented here consists of all EPIC-pn *XMM-Newton* observations of the extended 12MGS (Rush et al. 1993) that were public in the *XMM-Newton* data archive as of December 2008, including sources

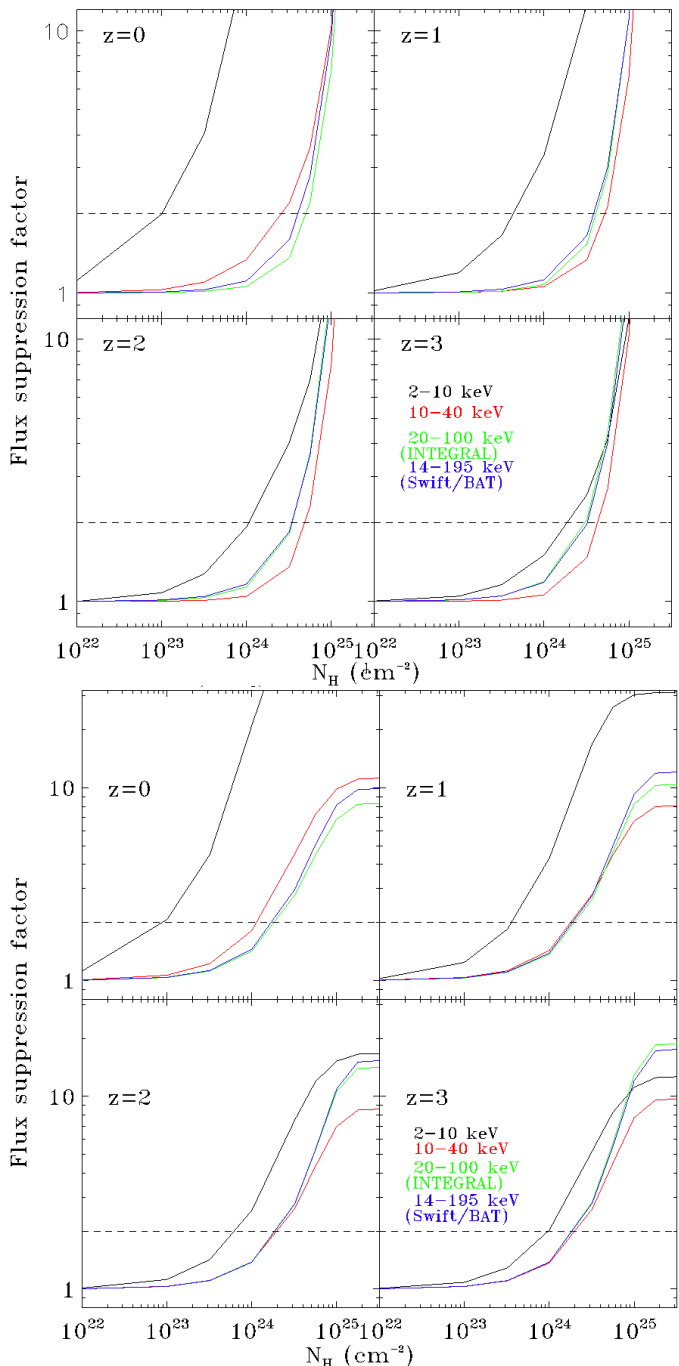


Figure 4. The flux suppression factors for the spherical model (top) and the torus model (bottom) for the observed frame 2-10 keV, 10-40 keV, 20-100 keV (INTEGRAL) and 14-195 keV (Swift/BAT) bands as a function of N_{H} at redshifts of 0, 1, 2 and 3. The flux suppression factor is defined as the unabsorbed flux in that band divided by the observed flux, for $\Gamma = 2$.

which were observed serendipitously. In the case of multiple observations of the same source, we use the longest observation available. The data were reduced homogeneously and systematically using the method described by Nandra et al. (2007) using *SAS* v7.0 tasks. This involves extraction of source events from a circular region, radius 35 arcsecs, centred on the source position, and extraction of background

events from rectangular regions, ensuring no contamination from interloping sources. We search for pileup effects in the observations by comparing the distribution of single and double pixel events, which are sensitive to these effects, to model distributions. Pileup effects are reduced if and when detected, by using only CCD pattern 0 (single) events (Ballet 1999). Background flares are filtered out by calculating the level of the background count rate at which the excess variance is determined to be zero. A background count rate of twice this level is used to filter the observation of flares. The subsequent background-subtracted spectra extracted are then binned with a minimum of 20 counts per bin, appropriate for χ^2 fitting. We include for analysis only those sources for which a meaningful spectrum has been produced by this process. This excludes those observations for which the flaring of the background has rendered the observation useless, where the source has not been detected above the background, or the detection is at low significance. We determine a meaningful spectrum to be one where the normalisation of a simple power-law model can be constrained to be greater than zero ($\Delta\chi^2 > 2.71$) with a fit to the 0.2-10 keV spectrum. After these considerations, the sample consists of 126 observations. The names, positions and redshifts of these galaxies along with the details of the *XMM-Newton* observations are given in Table 2. This set of *XMM-Newton* observations is quite varied, with exposures varying from hundreds of seconds to tens of kilo-seconds (Fig. 5), with differing observation modes and filters used. We do however, treat each spectral fit the same, regardless of the number and distribution of counts in the spectrum (see Fig. 5 for distribution of counts in these observations and the observed flux distribution).

3.2 Spectral fitting method: 2.5-10 keV

We use *XSPEC* v11.3 to carry out the spectral fitting of the 12 micron selected galaxies. As each spectrum has been grouped with a minimum of 20 counts per bin, the errors on the data points can be considered as Gaussian, and therefore χ^2 fitting can be used to find the best fit parameters for a given model.

Factors complicating the determination of the intrinsic parameters and the N_{H} are the soft excess components, ubiquitous in the soft X-ray spectra of AGN, which may arise from the accretion disk, thermal emission, scattered intrinsic emission and/or unresolved emission lines. For this reason, where possible, we determine the intrinsic source parameters from a fit to the 2.5-10 keV spectra for these galaxies, where the soft excess components are negligible. The following is a description of the spectral fitting methods we use.

We begin by fitting the 2.5-10 keV spectrum with a simple power-law model (`powerlaw` in *XSPEC*). We then systematically include further model components in order to fit the more complex features that the spectrum presents. We note the change in the χ^2 value of the fit after the addition of each added component and the change in the number of degrees of freedom (DOF). For a model combination to be allowed, we stipulate that $\Delta\chi^2 \geq 4.0$ for each DOF lost in adding the additional component (based loosely on 95% confidence levels quantified using an F-test). The combination of model components which meets these criteria and has the

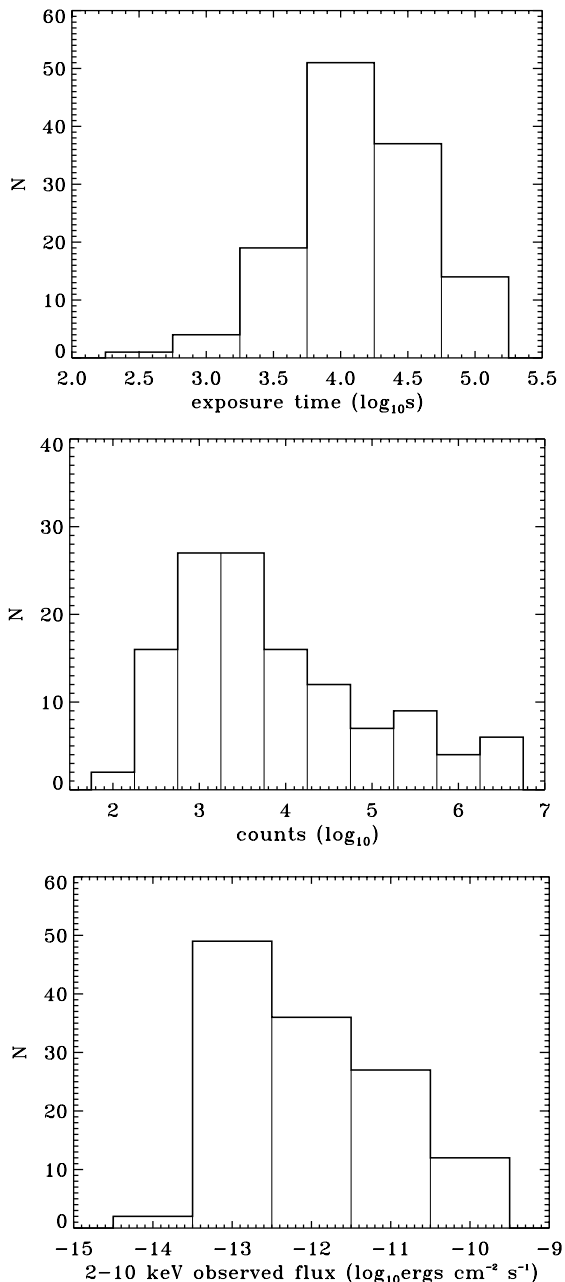


Figure 5. X-ray observation statistics for the sample, with exposure time distribution (top), source count distribution (middle) and observed source 2-10 keV flux (bottom)

smallest reduced χ^2 ($\chi_r^2 = \chi^2/\text{DOF}$) is presented as our best systematic fit for that spectrum.

We use the following models in combination to acquire a fit to the 2.5-10 keV spectrum:

- Neutral absorption model, `zwabs` (Morrison & McCammon 1983), for absorption intrinsic to the source.
- Neutral reflection from Compton thick material, `pexmon` (Nandra et al. 2007), which is derived from the `pexrav` model of Magdziarz & Zdziarski (1995) and includes self consistent Fe $K\alpha$, with its Compton shoulder, and Fe $K\beta$ line emission (George & Fabian 1991; Matt 2002).

- Our new model describing a heavily absorbed power-law, **trans**, based on Monte-Carlo calculations, with a spherical geometry, which take into account Compton scattering and includes line emission (as described in Section 2). We use this model in addition to the **zwabs** model as it is more likely to pick out a heavily obscured source due to the inclusion of line emission.

- Additional line emission, modelled by a gaussian:

The **pexmon** and **trans** models include Fe $K\alpha$ line emission, produced by cold distant matter, and therefore, if a narrow emission feature exists at 6.4 keV, these models should be preferentially included in the fit. We also check to see if any emission is present from ionised iron by adding narrow gaussians at 6.7 and 6.96 which correspond to $K\alpha$ emission from He-like and H-like iron respectively. We also add a third gaussian component with energy constrained to be $6.2 < E_{line} < 6.6$ keV and with a free width parameter, to check for broad Fe $K\alpha$. This represents $\Delta E = 0.2$ keV from the rest-frame energy of neutral Fe $K\alpha$ so as to avoid fitting ionised Fe lines at higher energy. In reality, broad Fe $K\alpha$ lines have been found with a lower energy than the energy we permit (e.g. Nandra et al. 2007), but we use this conservative range as broad Fe $K\alpha$ lines are not the focus of this investigation. We keep these gaussian components if the normalisation of each line is constrained to be greater than zero ($\Delta\chi^2 > 2.71$).

We keep the power-law indices for the **pexmon** and **trans** components equal to the primary power-law for each fit as it is presumed that each component in this band has the same origin. For spectra where the power-law index, Γ , is badly constrained we fix the power-law index to $\Gamma = 1.9$, the canonical value for Seyfert galaxies (Nandra & Pounds 1994), which make up the majority of our sample, but also roughly appropriate for galaxies (Ptak et al. 1999). We define fits where Γ cannot be constrained within $\Delta\Gamma \leq 0.7$ to be unconstrained as such an uncertainty introduces a large overall uncertainty into the fit and other fit parameters as well as the source luminosity.

We fit the 2.5-10 keV spectra initially as this band is least affected by galactic and other complex soft X-ray emission, and is therefore best suited for determining the intrinsic parameters of the nuclear source. Furthermore, the higher signal-to-noise ratio at soft energies often results in spectral fits being driven by the soft features. For example, strong soft emission may cause the power-law index to steepen and as a result the measured N_H may increase to compensate for this. However, the lower signal-to-noise ratio in the hard band can sometimes lead to unconstrained fits. We do not use fits where the normalisation of the power-law is not constrained to be greater than zero and instead use the full band fit method, described below. For fits that produce a low Γ , a hidden transmission or reflection component is likely to be present and not recognised by the 2.5-10 keV fit. Where $\Gamma < 1.4$, this presents a scenario where the photon index lies greater than $3\text{-}\sigma$ away from the mean measured by Nandra & Pounds (1994). In this case we also refer to the full band fit, where a reflection or heavily obscured transmission component is often then detected.

3.3 Spectral fitting method: 0.2-10 keV

Ignoring data below 2.5 keV leaves us insensitive to neutral columns less than $\sim 10^{22}$ cm $^{-2}$. For satisfactory hard band fits, we then freeze the hard band fit and continue fitting the 0.2-10 keV spectrum with these parameters frozen, with the exception of the N_H parameter. The following models are then systematically added, again requiring that $\Delta\chi^2 \geq 4.0$ for each degree of freedom lost in adding the additional component. Again, the combination of model components which meets these criteria and has the smallest reduced χ^2 ($\chi_r^2 = \chi^2/\text{DOF}$) is adopted as our best systematic fit for the 0.2-10 spectrum.

- Neutral absorption (**wabs**) associated with the Galaxy, frozen to the value given in Table 3 and applied to the whole spectrum. This component is assumed to be present regardless of the $\Delta\chi^2$.

- Absorption applied to the whole spectrum and intrinsic to the host galaxy, be it neutral or ionised (see below). If no neutral absorption is detected in the hard band, we also check to see if a neutral absorption component is required for the primary power-law in the soft band (**zwabs**).

- A warm absorber (**cwa18**, based on XSTAR (Kallman et al. 2004). See Nandra et al. (2007) and references therein for description) to model cases where ionised absorption features are present in the spectrum. If evidence for neutral absorption is present in the hard band fit, we also check whether an improved fit results by adding a warm absorber on top of this or indeed, replacing this with a warm absorber.

- A thermal plasma component (**apec**, Smith et al. 2001). The soft X-ray spectra of obscured AGN have been shown to consist partly of emission lines photo-ionised by the AGN (Guainazzi & Bianchi 2007). Models such as **apec** are often used to account for this emission when these lines are not resolved. When using this model, the abundances are initially frozen to the solar values, however, once the best fit is obtained, we check if thawing the abundances produces a better fit.

- A second power-law, where the power-law index, Γ_2 is constrained such that $\Gamma_2 = \Gamma_1$. This component is used to fit any ‘scattered power-law’ often seen in Seyfert 2 type spectra (Turner et al. 1997). It can only be seen when moderate or high absorption is occurring to the primary power-law, and therefore we only add it if absorption is detected in the hard band fit.

- We also check to see whether $\Gamma_2 \geq \Gamma_1$ produces a better fit.

3.3.1 Modelling the soft-excess seen in Seyfert 1 like spectra

Modelling the soft-excess seen in quasar and Seyfert 1 like spectra is complicated, especially as we do not fully understand the nature of this feature. The models used to fit the soft excess are additive (often a blackbody or Comptonised component), thus accounting for flux in the soft X-ray band. However, if an absorption component is used in conjunction, adding the soft excess component can lead to an over-estimation of the N_H parameter due to ‘balancing’ of emission and absorption. Thus, we apply strict criteria in order to include a soft excess model in the spectral fit.

This soft excess is thought to originate from close to the

central engine, and thus should be an excess above the intrinsic, *unabsorbed* power-law spectrum. To test for the soft excess, we extrapolate our fit of the 2.5-10 keV spectrum into the soft band, removing any absorption components. Only then, if there is emission in excess of this extrapolated fit in the soft band, do we include soft-excess components in the soft band fit. To detect excess emission in the soft band, we use a ‘soft ratio’, defined as the data-to-model ratio at 0.4 keV, done similarly by Sobolewska & Done (2007). An energy of 0.4 keV is used to avoid atomic emission from oxygen at ~ 0.7 keV. We choose a soft ratio lower cut off of 1.2 (20%), which is high enough to exclude uncertainties in the spectral calibration (see below). We also require this ratio to be rising towards softer energies, as emission from thermal plasmas can cause an excess at 0.4 keV, but that peaks at higher energy. Figure 6 gives two examples where this soft ratio is greater than 20%, but one shows a classical soft excess which rises from 1 keV to 0.5 keV (3C273), whereas the other shows an excess due to the emission from a thermal plasma, which falls from 1 keV to 0.5 keV (Messier 100). If the soft ratio exceeds 1.2 and the ratio is rising from 1 to 0.5 keV, we then proceed to include soft excess model components in the spectral fit. The model components we use to fit the soft excess are either a black body (`bbody`) or a Comptonised (`compTT`) component, whichever provides the best fit.

3.3.2 Bad spectral fits

We define fits which give $\chi_r^2 > 2.0$ as ‘bad’. Although this definition is arbitrary, it is useful for identifying cases where the models used are not a good representation of the spectrum. For the 2.5-10 keV fits, only NGC 1068, NGC 1365 and M82 have bad fits. These sources have notoriously complex spectra, which are high signal to noise in this case, with several emission and absorption features. We do not attempt to fit these additional complexities, however, and present only the basic hard band parameters for these fits. No errors are quoted because the standard formalism does not apply unless the model fits the data (Lampton et al. 1976).

When we fit the full band spectrum, we sometimes find that keeping the hard band parameters fixed will cause a bad full band fit, so we then thaw these parameters for an improvement. After this procedure, 17/126 fits are still bad. These bad fits usually result from high signal-to-noise spectra which reveal highly structured soft X-ray features which are too complex for our models. However, the nature of the soft X-ray emission is not the focus of this investigation, as we seek mainly the intrinsic hard X-ray power of the source, along with any neutral absorption present. In these cases, we do not present the results from the full band fit, rather only the hard band fit. These are denoted by an ^(H) in the spectral fit table. Furthermore, we note that the calibration uncertainties on *XMM-Newton* are at the level of $\sim 5\%$ (Kirsch et al. 2004). If the ratio of the data to the model is less than this in the soft band, the bad fit may be partially due to calibration uncertainties. In this case we present the soft band fit results, despite a bad χ^2 . We present the parameters Γ and the power-law normalisation from the hard band fits here as these fits had ‘good’ χ_r^2 values and thus the uncertainties could be estimated. These are denoted by

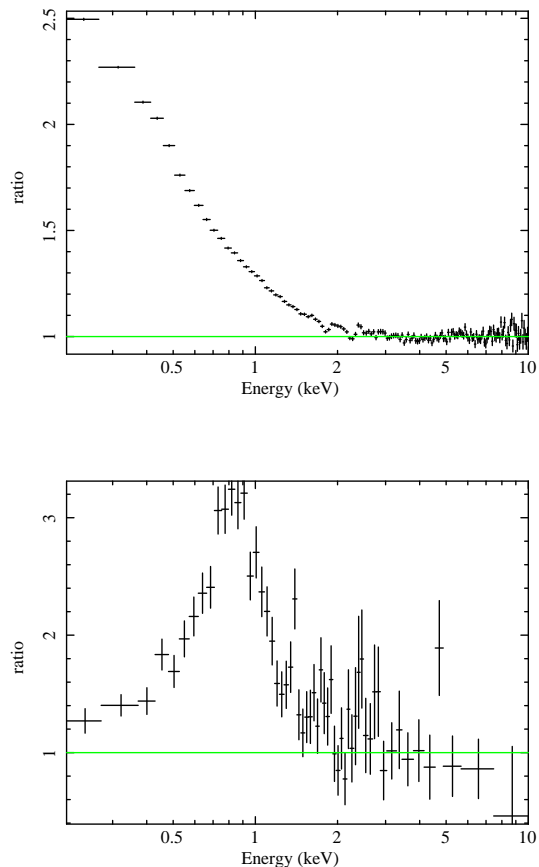


Figure 6. The ratio of the data to the extrapolated 2.5-10 keV power-law for 3C273 (top) and Messier 100 (bottom). 3C273 has a classical soft excess at up to more than twice the level of the extrapolated power-law. Messier 100 has strong emission from a thermal plasma, but this peaks at ~ 1 keV.

a ^(D) in the spectral fit table. 3C120 is an example of a source with a bad spectral fit, but a data/model ratio of less than 5%, which we show as an example in Fig. 8. Our procedure should not result in grossly inaccurate estimates of Γ , L_X or N_H in such cases.

For cases where the hard band fit is unconstrained (i.e. the power-law normalisation is not constrained to be greater than zero) or the hard band fit is bad ($\chi_r^2 > 2.0$), then we cannot use the method described above, whereby the hard band fit is extended into the soft band. In these cases, we carry out simultaneous full, 0.2-10 keV band fits with all model components. Although this is less desirable, it is useful in the case where the hard band fit is unsatisfactory and for cases where the hard band measures a flat power-law index. These are denoted by an ^(F) in the spectral fit table.

3.4 Intrinsic power and reflection fraction

We calculate the intrinsic power emitted in the 2-10 keV band for each galaxy based on the absorption corrected flux in the 2-10 keV band from the spectral fits to the primary power-law. We define the primary power-law as the power-

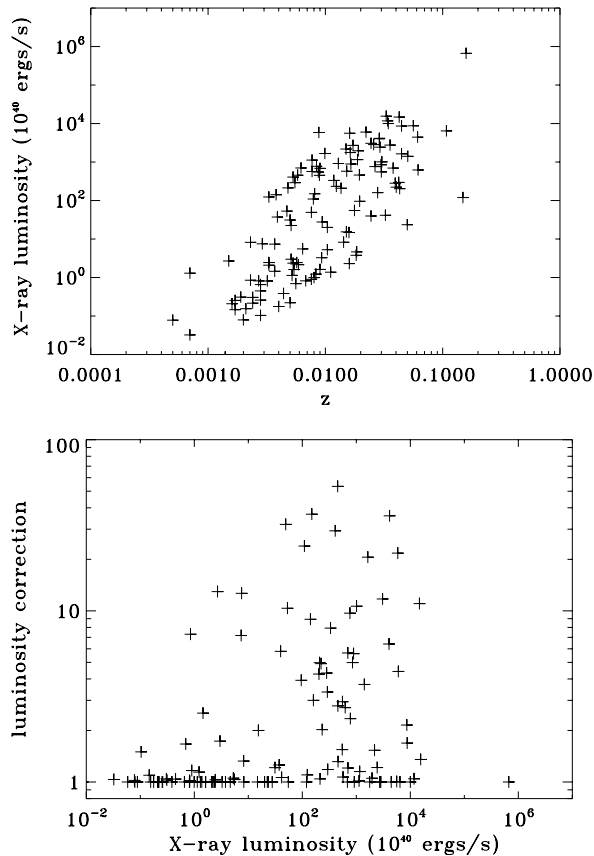


Figure 7. (top) 2-10 keV intrinsic (absorption corrected) luminosity plotted against redshift for all objects. (bottom) The luminosity correction ($L_X(int)/L_X(obs)$) against the intrinsic X-ray luminosity.

law component with the greatest normalisation, i.e. the intrinsic flux at 1 keV. This may include the **trans** component, if this is present, which will typically model a heavily obscured hard component visible only at hard energies. Standard cosmological parameters are assumed throughout ($\Omega_m = 0.3$, $\Lambda = 0.7$, $H_0 = 70 \text{ km s}^{-1} \text{ Mpc}^{-1}$). In the top panel of Fig. 7 the intrinsic, absorption corrected 2-10 keV luminosity of each galaxy is plotted against its redshift. This figure illustrates that the 12MGS is a low redshift galaxy sample, with a wide range of X-ray luminosities from $10^{38} \text{ ergs}^{-1}$ through to $10^{44} \text{ ergs}^{-1}$ (though with one very luminous source, 3C273 at $\sim 10^{46} \text{ ergs}^{-1}$). The lower panel shows the size of the correction made to the observed luminosity against the intrinsic luminosity, which can be up to a factor of ~ 50 .

For reflection dominated spectra, we derive the intrinsic power of the source from the intrinsic power-law required to produce the reflection component. The **pexmon** model calculates the reflection from a semi-infinite slab, subtending 2π steradians on the sky. The estimate of the intrinsic power in the reflection dominated sources is uncertain as it depends on the precise geometry of the reflector. This was shown by Murphy & Yaqoob (2009) who modelled reflection from a toroidal distribution of matter, finding that the reflection fraction can be underestimated in this way by a factor of

~ 6 . We also investigate the reflection fraction and intrinsic luminosity derived using the **pexmon** model and compare these to those derived from our own **torus** model.

3.5 What can we determine using the torus spectral model?

For spectra in which we find reflection is strong ($R_{pexmon} > 1$, where R_{pexmon} is the ratio of the normalisation of the **pexmon** component to the normalisation of the primary power-law), we fit the same spectrum with model spectra from the torus simulations with two aims. Firstly, as mentioned above, we aim to investigate the reflection fraction and intrinsic source luminosity as determined using the torus model with respect to the **pexmon** slab model, and secondly, we investigate if it is possible to determine and constrain the torus geometric parameters, θ_{tor} and θ_i from the 2-10 keV spectra. For determining the reflection fraction, we fix $\theta_{tor} = 60^\circ$, leaving θ_i free to vary. We then determine if the inclination angle can be constrained. Following this, we fix $\theta_i = 90^\circ$, and allow θ_{tor} to vary, to see if this can be constrained.

3.6 X-ray AGN in our sample

The main goal of this work is to ascertain the properties of the primary emission, as well as the absorption characteristics of our sample. We do this initially for our whole sample, and we then go on to do so for AGN only. We define a set of unambiguous X-ray AGN as galaxies with an observed 2-10 keV luminosity greater than $10^{42} \text{ ergs}^{-1}$ as these sources are unambiguously powered by the accretion of material onto a super-massive black hole. No local pure star-forming galaxy has ever presented a 2-10 keV luminosity above this limit. One of the most X-ray luminous star forming galaxies is NGC 3256, which presents a 2-10 keV luminosity of $2.5 \times 10^{41} \text{ ergs}^{-1}$, but shows no evidence for AGN activity (Moran et al. 1999). Therefore, galaxies with an observed 2-10 keV luminosity greater than $10^{42} \text{ ergs}^{-1}$ are very likely to host an AGN. However, this will not select all AGN in this sample, so the remaining sources cannot be thought of as non-AGN. In this way $60/126=48\%$ of the sources in our sample are unambiguous AGN taking into account their X-ray luminosities only.

4 SPECTRAL FITTING RESULTS

4.1 Spectral fit components and parameters

From our spectral fitting method, we have determined a best fit model for each source, which includes all the absorption and soft excess components, giving us an accurate estimate of Γ , N_H and the intrinsic power accounting for the complexities in the spectra. For 126 spectra, we find that in 62 of them, we can constrain Γ on the primary power-law to $\Delta\Gamma < 0.7$ (we fix $\Gamma = 1.9$ otherwise). Furthermore, 96 spectral fits require an absorption component, 39 of which warm absorption has been detected. A thermal plasma component is ubiquitous in the fits as well, needed to fit 93 spectra. Fe $K\alpha$ emission is detected in 71 spectra, where 36 of these

are broad lines ($\sigma > 0.1$ keV). A secondary power-law component is required in 44 of our fits, and reflection is also required in 44 of the fits.

The spectral parameters of all fits are listed in Tables 3 to 8. Table 3 presents the basic spectral fit parameters such as the fit statistics, the parameters of the primary power-law and the thermal plasma component, where present, and the observed 2-10 keV flux and intrinsic 2-10 keV luminosity. Table 4 gives details of any secondary power-law component required in the fit; Table 5 gives details of the sources which have a soft excess detected and of the models used to fit this component; Table 6 presents details of the reflection component needed in each fit, including data obtained from the `torus` model; Table 7 presents the parameters of the warm absorber model if ionised absorption has been detected in the spectrum; and Table 8 gives details of the line emission detected in the iron K regime. Included on all fit parameters in which a satisfactory fit has been acquired are the 90% confidence errors for one interesting parameter ($\Delta\chi^2=2.706$).

A selection of example spectra are presented in Fig. 8. These are the spectra of 3C120, NGC 3079, NGC 4593, NGC 5170, UGC08850 and NGC7479, chosen to display a range in signal-to-noise ratio as well as model components. 3C120 and NGC 4593 have a soft excess present in their spectra as determined by the ratio of the data at 0.4 keV to the extrapolated 2.5-10 keV power-law, and fitted by the `compTT` model. Reflection from neutral material is included in the fit, where in the case of NGC 4593, this component accounts for the Fe K α emission seen. 3C120 requires an additional gaussian component to model what seems to be broad Fe K α emission. These fits also include a thermal plasma component, however, it is possible that in these cases this model component is not representative of real thermal plasma emission as this component is not likely to be detected above the emission from the AGN, and is rather being used to fit the soft complexities of the spectra. A warm absorber has also been detected in the spectrum of NGC 4593.

The spectrum of NGC 3079 is typical of a reflection dominated spectrum ($R_{\text{pexmon}} = 16.3$) with an intense Fe K α component (940 eV) and is certainly Compton thick. UGC 08850 presents a transmission dominated spectrum, which is well fitted by our new model `trans` measuring $N_{\text{H}} = 3.8 \times 10^{23} \text{ cm}^{-2}$, plus a scattered power-law. In the spectrum of NGC 7479 we have detected a hidden transmission component ($N_{\text{H}} = 2 \times 10^{24} \text{ cm}^{-2}$) beneath a reflection dominated spectrum, though it is not well constrained. The dominance of the reflection component and high EW of the Fe K α line (768 eV) imply a high column density in support the measured N_{H} in the transmission component.

The spectrum of NGC 5170 has a low signal to noise ratio and in this case we have had to fix the power-law index to 1.9. The only added model component here is low level neutral absorption.

In Fig. 9, we present the 2.5-10 keV spectrum of NGC 1068, which is an example of where the 2.5-10 keV fit is bad. This is a high signal-to-noise spectrum which reveals multiple discrete features, possibly due to absorption and emission, or even calibration uncertainties.

4.2 Properties of the primary emission

The primary power-law is found to have a mean power-law index, $\langle \Gamma \rangle = 1.90_{-0.07}^{+0.05}$ for the whole sample, and an intrinsic spread of $\sigma = 0.31_{-0.05}^{+0.05}$. We use the maximum likelihood method of Maccacaro et al. (1988), which takes into account the measurement errors on Γ , to determine both the mean and the intrinsic standard deviation of this distribution.

We also investigate the Γ distributions for obscured and unobscured sources, which is an important test for AGN unification. We do this for the entire sample, and also for unambiguous AGN with $L_{\text{X}} > 10^{42} \text{ erg s}^{-1}$. In Fig. 10 we show how the distribution of Γ differs for obscured sources in these two cases. We again use the maximum likelihood method of Maccacaro et al. (1988) to determine both the mean and the intrinsic standard deviation for each of these distributions. We find that for all unobscured sources, $\langle \Gamma \rangle = 1.90_{-0.09}^{+0.09}$ and $\sigma = 0.33_{-0.06}^{+0.07}$ and for all obscured sources, $\langle \Gamma \rangle = 1.97_{-0.12}^{+0.14}$ and $\sigma = 0.44_{-0.09}^{+0.12}$. This is statistically consistent with the intrinsic power-law indices of these two populations being the same. We also find that for unobscured AGN, $\langle \Gamma \rangle = 1.84_{-0.14}^{+0.12}$ and $\sigma = 0.32_{-0.08}^{+0.11}$ and for obscured AGN, $\langle \Gamma \rangle = 1.90_{-0.14}^{+0.16}$ and $\sigma = 0.38_{-0.07}^{+0.13}$. This is again statistically consistent with the intrinsic power-law indices and their intrinsic spreads being the same for both obscured and unobscured AGN. A Kolmogorov-Smirnov (K-S) test confirms that the probability that these distributions are drawn from different parent samples is low (42%) for AGN.

Furthermore, we find no dependence of Γ on X-ray luminosity. We show this in Fig. 11 in the range of 10^{38} to $10^{45} \text{ erg s}^{-1}$, where the scatter of Γ versus X-ray luminosity is plotted, as well as the mean values for each logarithmically spaced luminosity bins. The vertical error bars show one standard deviation spreads in the values.

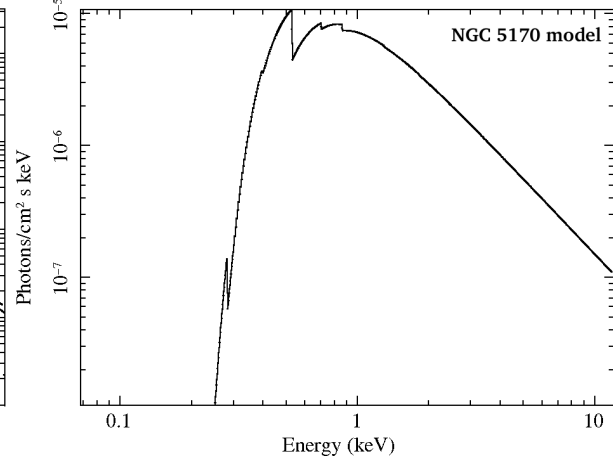
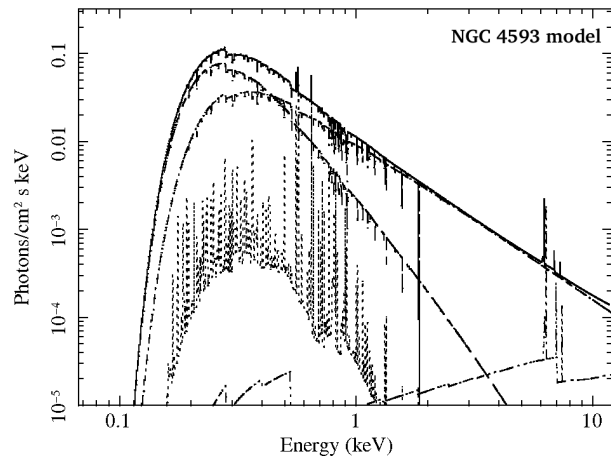
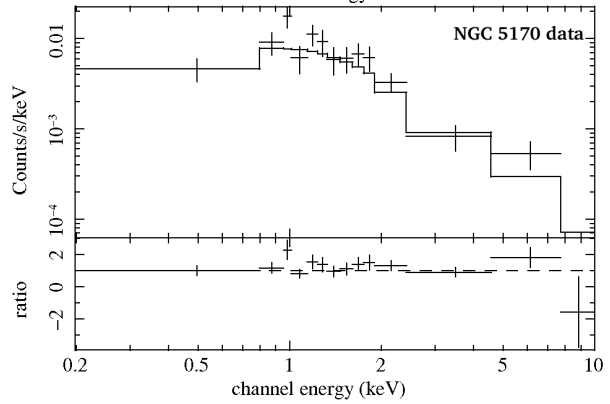
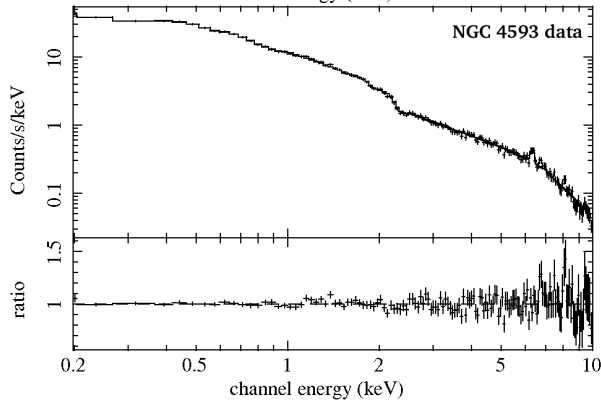
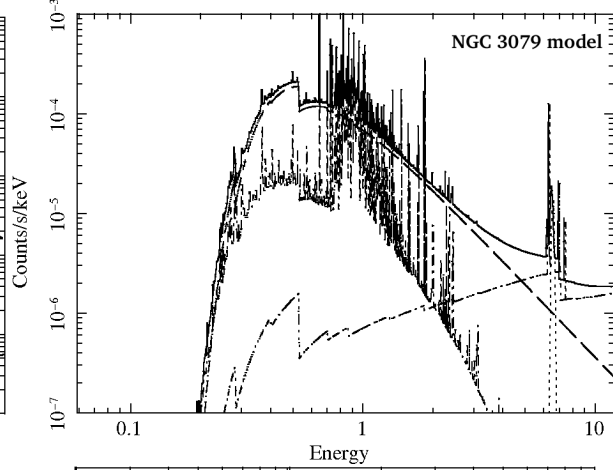
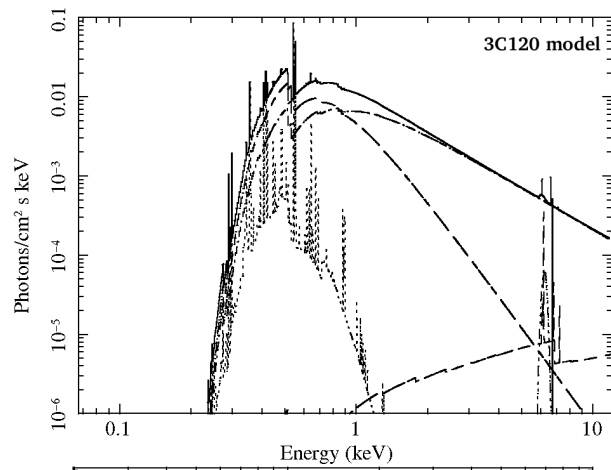
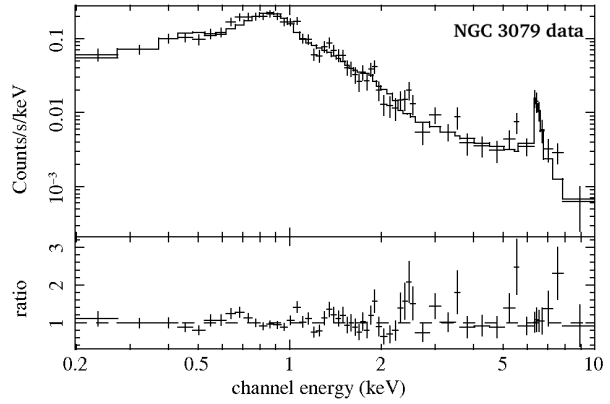
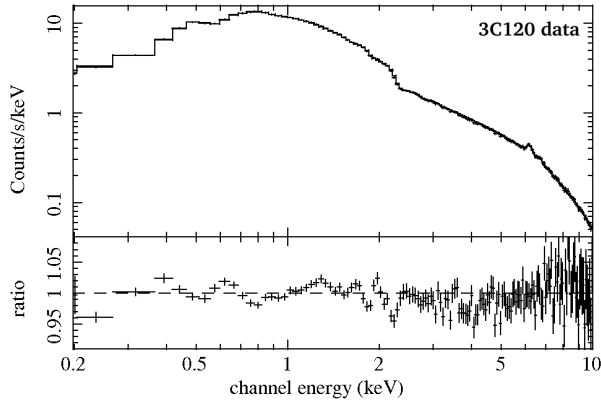
4.2.1 Soft-excess modelling

We find that a total of 15 spectra in our sample require a soft-excess model component in their spectral fit. We have determined this from two soft ratio criteria, that the soft ratio must be > 1.2 and that it must be rising from 1 keV to 0.5 keV. 3C120 has a soft excess which does not fit our criteria, as it does not have a data/model ratio greater than 20% at 0.4 keV. However, this source has a clear soft excess at 0.7 keV not well modelled by thermal plasma emission. We find that a ratio of 3.2 at 0.4 keV is recovered when an additional intrinsic absorption component is used. In Fig. 12, we plot the distribution of the soft ratio, which ranges from ~ 1.3 -7.8 for our sample, though with only one spectrum with a ratio greater than 4. Sobolewska & Done (2007) note that this soft ratio ranges from ~ 2 -3 for their sample of quasars. The details of these fits are presented in Table 5. All but three of the fits prefer a Comptonised component over a black-body component.

4.3 Obscuration and reflection

4.3.1 Compton thin sources

We find that 28/126 (22%) of our spectra show no evidence for any absorption at all, whereas 77 (61%) spectra present



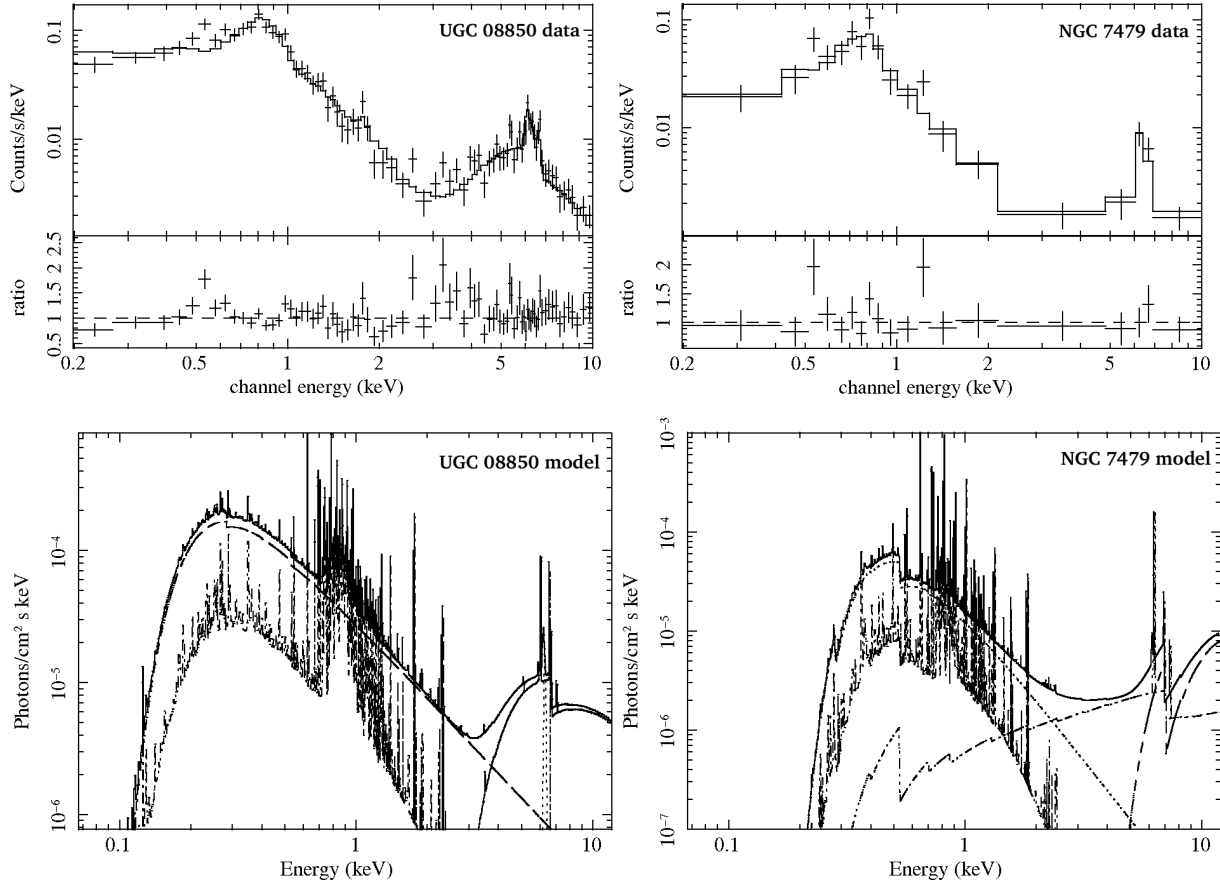


Figure 8. 0.2-10 keV spectra of 3C120, NGC 3079, NGC 4593, NGC 5170, UGC08850 and NGC7479, shown with best fit model from Table 3.

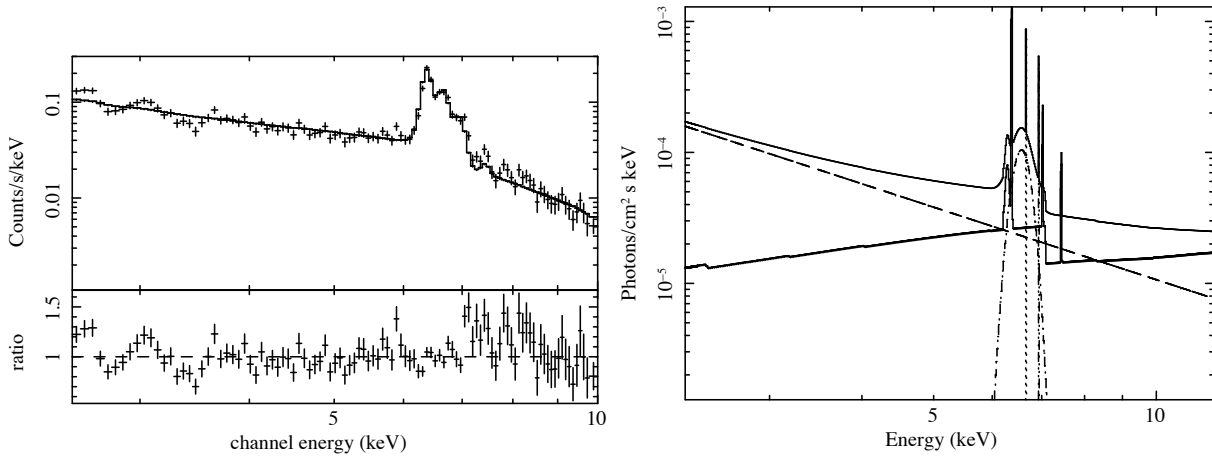


Figure 9. 2.5-10 keV spectrum of NGC 1068 (left), shown with best fit model (right) from Table 3. This is an example of a spectrum where the fit is bad due to spectral features too complex for the models we use.

Compton thin (neutral) absorption, showing that absorption is commonplace in the X-ray spectra of all galaxies.

4.3.2 Compton thick sources

As mentioned previously, for 0.2-10 keV X-ray spectra, a direct measurement of a column density of Compton thick

source is difficult due to the extreme suppression of the X-ray flux in this band. We have, however, successfully used our new model, *trans*, to directly measure the N_{H} to be greater than $1.5 \times 10^{24} \text{ cm}^{-2}$ in four sources (NGC 1320, NGC 1667, NGC 4968 and NGC 7479). The inclusion of a self-consistently modelled iron $K\alpha$ line is likely to have

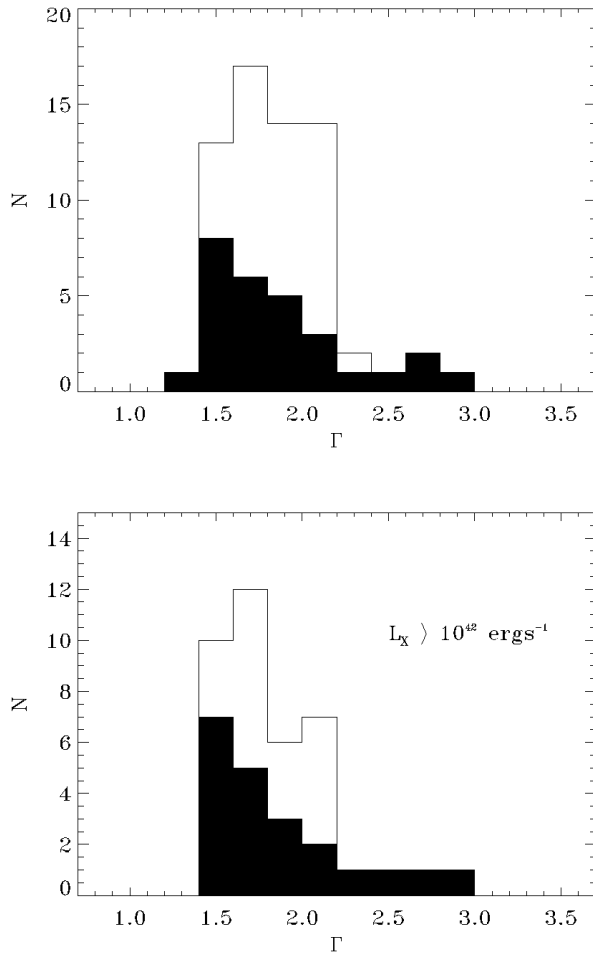


Figure 10. Top: Γ distribution of all sources (empty histogram), and obscured sources ($N_{\text{H}} > 10^{22} \text{ cm}^{-2}$, black histogram). Bottom: Γ distribution of all unambiguous AGN, defined by $L_{\text{X}} > 10^{42} \text{ ergs s}^{-1}$ (empty histogram), and obscured AGN ($N_{\text{H}} > 10^{22} \text{ cm}^{-2}$, black histogram). The Γ presented is that from the primary power-law only.

provided greater constraint on the N_{H} than models which include this component separately.

In our analysis, we call sources with a reflection dominated spectrum Compton thick, of which there are 12. We define a reflection dominated spectrum to be where $R_{\text{peaxmon}} > 8$. The $R_{\text{peaxmon}} > 8$ criterion is arbitrary and chosen to be low enough to include known Compton thick AGN such as NGC 1068. Figure 13 shows the EW of the Fe $K\alpha$ line against N_{H} for our sample for reflection dominated sources (green), mildly reflection dominated sources (blue, $1 < R < 8$) and sources with weak or no reflection (red, $R < 1$). It can be seen from this that reflection dominated sources also have high iron line EWs. We plot only narrow line EWs here, which are most likely to originate in cold distant obscuring matter, unless no narrow line has been measured, in which case we plot the broad line EW, if one has been measured

There are two sources, however, that have high iron line EWs which are constrained to be $> 300 \text{ keV}$, but have

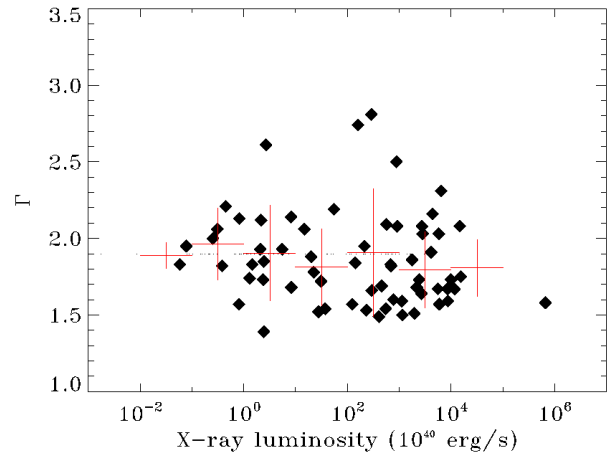


Figure 11. Plot of Γ vs. 2-10 keV intrinsic luminosity. Red crosses give the mean Γ for each luminosity bin. The vertical error bars show one standard deviation spreads in the values.

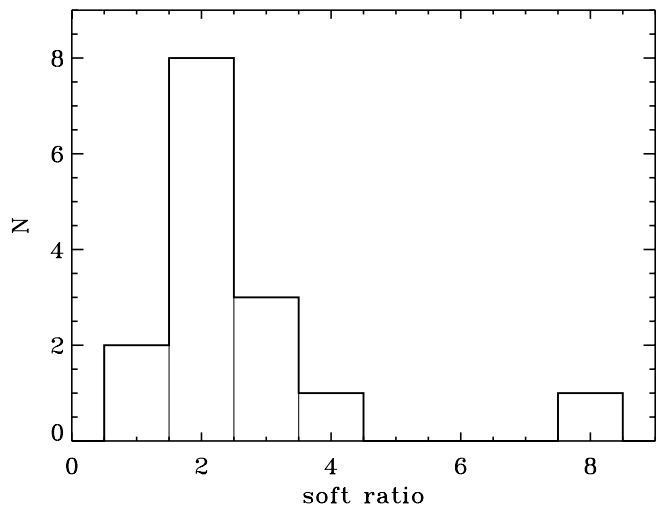


Figure 12. Distribution of the soft ratio, the data-to-model ratio at 0.4 keV to the extrapolated 2.5-10 keV power-law, for 15 sources found to have a soft excess.

a measured $N_{\text{H}} < 10^{22} \text{ cm}^{-2}$. Our Monte-Carlo simulations have shown that this is not possible for either a spherical or toroidal matter distribution, and so we investigate them further. These sources are NGC 3690 and IRASF13349+2438. NGC 3690 is the merging system ARP 299, which was shown by *Beppo-SAX* to host a Compton thick AGN (Della Ceca et al. 2002), confirming our assertion. We therefore add it to our sample of Compton thick AGN. Longinotti et al. (2003) examine the Fe $K\alpha$ features in the X-ray spectrum of IRASF13349+2438, a narrow-line Seyfert 1, finding them to be broad and complex. This line is therefore unlikely to originate from distant Compton thick obscuring matter. This shows that Fe $K\alpha$ EW diagnostics for obscuration are only suitable when we can be sure that the line originates in cold, distant matter such as the torus.

For sources where their Compton thick nature has been

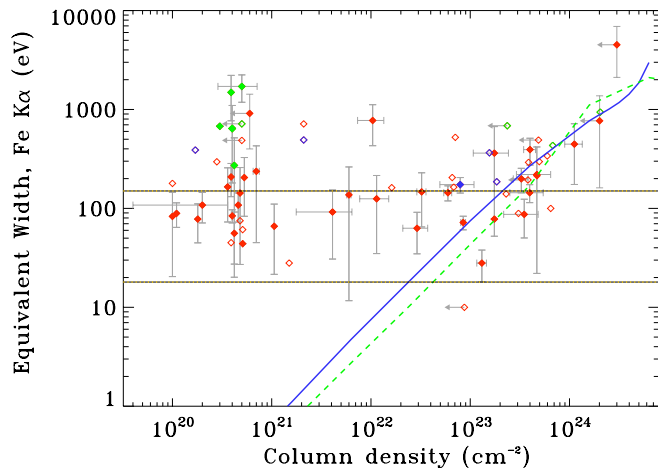


Figure 13. The equivalent width of iron $K\alpha$ line versus directly measured N_{H} for our sample. The lines drawn show the theoretical relationship between the EW of the Fe $K\alpha$ line and the N_{H} , calculated from the Monte-Carlo simulations, described in section 2 for a power-law with $\Gamma=2$ and solar abundances. The solid blue line shows the calculations for the spherical distribution, the dashed green line shows the calculations for the torus distribution for the equatorial line of sight, and a torus opening angle of $\theta_{\text{tor}}=60^\circ$. The dotted yellow lines show maximum and minimum EWs observed from unobscured sight lines in the torus distribution, taken from Fig 3, where the line of sight N_{H} through the torus is greater than 10^{23} cm^{-2} . Thus, all truly unobscured sources must have an EW less than the maximum shown. Sources which are reflection dominated ($R>8$) are shown in green. Sources with $1 < R < 8$ are shown in blue for comparison. All grey lines are error bars. These are only shown where the EW is consistent with being non-zero (plotted as filled diamonds, otherwise plotted as open diamonds). Arrows indicate upper limits on the N_{H} .

inferred by the EW and the reflection fraction, we can only put a lower limit on the N_{H} of $1.5 \times 10^{24} \text{ cm}^{-2}$, but in reality, this could be higher and requires data above 10 keV to constrain. We find a total of 16 Compton thick sources in our sample, the details of which are given in Table 10. The Compton thick fraction for all 126 galaxies is 16/126 ($=13 \pm 3\%$), where the errors have been calculated for a binomial distribution ($\sigma_p = \sqrt{p(1-p)/N}$, where p is the proportion and N the total number of sources). The Compton thick fraction for unambiguous AGN ($L_{\text{X}} > 10^{42} \text{ erg s}^{-1}$) is 11/60 ($=18 \pm 5\%$).

4.3.3 N_{H} distribution and obscured fraction

In Fig. 14, we present the N_{H} distribution for the whole sample, and over-plotted is the N_{H} distribution of those with $L_{\text{X}} > 10^{42} \text{ erg s}^{-1}$. The main difference in the two distributions is the strong peak of unobscured sources at low X-ray luminosities and the greater proportion of heavily absorbed X-ray luminous AGN. The low luminosity, unabsorbed sources may consist of unobscured star forming galaxies, LINERs or lower luminosity AGN, but we will investigate this further in paper II. The N_{H} distribution of unambiguous AGN shows a smaller unobscured peak, but with a second obscured peak at $N_{\text{H}}=10^{23-24}$.

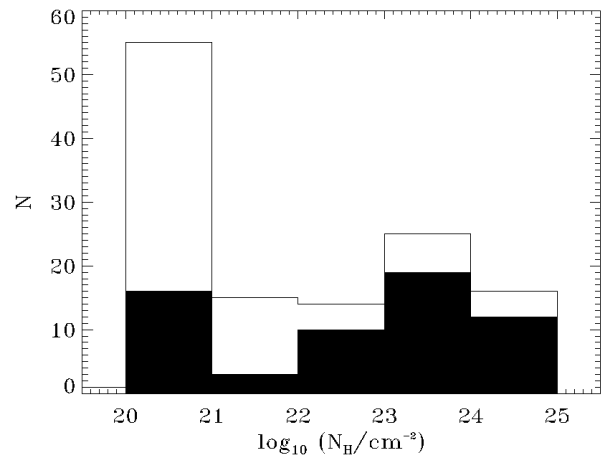


Figure 14. N_{H} distribution of all sources (empty histogram), and unambiguous AGN, defined by $L_{\text{X}} > 10^{42} \text{ erg s}^{-1}$ (black histogram). The N_{H} presented is that measured from the primary power-law only.

Fig. 15 plots N_{H} vs. L_{X} and also the obscured fraction, defined as the ratio of the number of sources with $N_{\text{H}} > 10^{22} \text{ cm}^{-2}$ to the total number of sources in each luminosity bin. There is significant variation in the obscured fraction with X-ray luminosity, particularly above and below $10^{42} \text{ erg s}^{-1}$ where the ratio declines steeply from a peak.

4.3.4 Reflection dominated sources

For sources where the X-ray spectrum includes a strong reflection component, we have also fitted our new torus model, firstly to investigate the reflection fraction and intrinsic source luminosities as determined using this model with respect to the `pexmon` slab model. Secondly, we investigate if it is possible to determine the torus geometric parameters, θ_{tor} and θ_i from the 2-10 keV spectra. In Fig. 16 we plot the distributions of the ratio of the reflection fraction as determined by the `torus` model to the reflection fraction determined by the `pexmon` model and the ratio of the intrinsic luminosities as determined by each model. We find that for most sources, both the reflection fraction and intrinsic source luminosity as determined using the torus model is greater than that determined by the `pexmon` model. The means and medians of these ratios are 3.08 and 2.70 for $R_{\text{torus}}/R_{\text{pexmon}}$ and 2.62 and 1.99 for $L_{\text{Xtorus}}/L_{\text{Xpexmon}}$. We also find that it is not possible to constrain the inclination angle or opening angle of the torus with these data below 10 keV, as neither parameter can be constrained, even with the other parameter fixed.

5 DISCUSSION

5.1 X-ray transmission in heavily obscured sources

We have made predictions of the equivalent width (EW) of the iron line for different model parameters and for two matter geometries, a sphere and a torus. The predictions

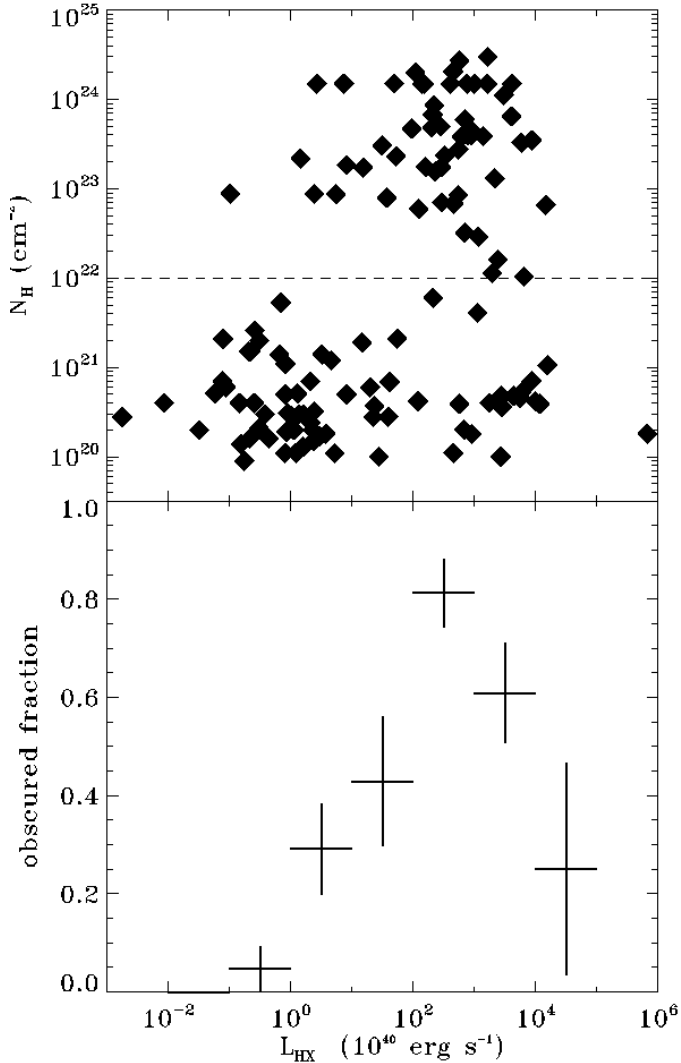


Figure 15. N_{H} and obscured fraction versus 2-10 keV luminosity for all sources. Obscured fraction is calculated in equal logarithmic luminosity bins, as the number of sources with $N_{\text{H}} > 10^{22} \text{ cm}^{-2}$ divided by the total number of sources in that bin, where more than one source exists per bin.

we make for the torus are useful for comparing observed EWs and making inferences from these about the matter geometry and parameters in the observed system. For example, we find that a maximum EW of 150 eV is achievable when considering a torus geometry for unobscured sightlines with a typical Γ (2.0) and solar abundances. To achieve greater EWs than this, the line of sight must be obscured with $N_{\text{H}} > 10^{23} \text{ cm}^{-2}$. Therefore, if an EW higher than this is measured for an unabsorbed spectrum, it may cast doubts on the reliability of the measured line of sight N_{H} . We showed this for NGC 3690, which shows an Fe K α EW of 913_{-346}^{+380} eV, but a measured N_{H} of only $6.14_{-6.14}^{+5.57} \times 10^{20} \text{ cm}^{-2}$ which is clearly at odds with our model predictions. Data above 10 keV from *Beppo-SAX* shows, however, that this source is indeed heavily obscured with $N_{\text{H}} > 1.5 \times 10^{24} \text{ cm}^{-2}$ (Della Ceca et al. 2002), in full support of our model predictions. Our Fe K α EW predictions also agree well with

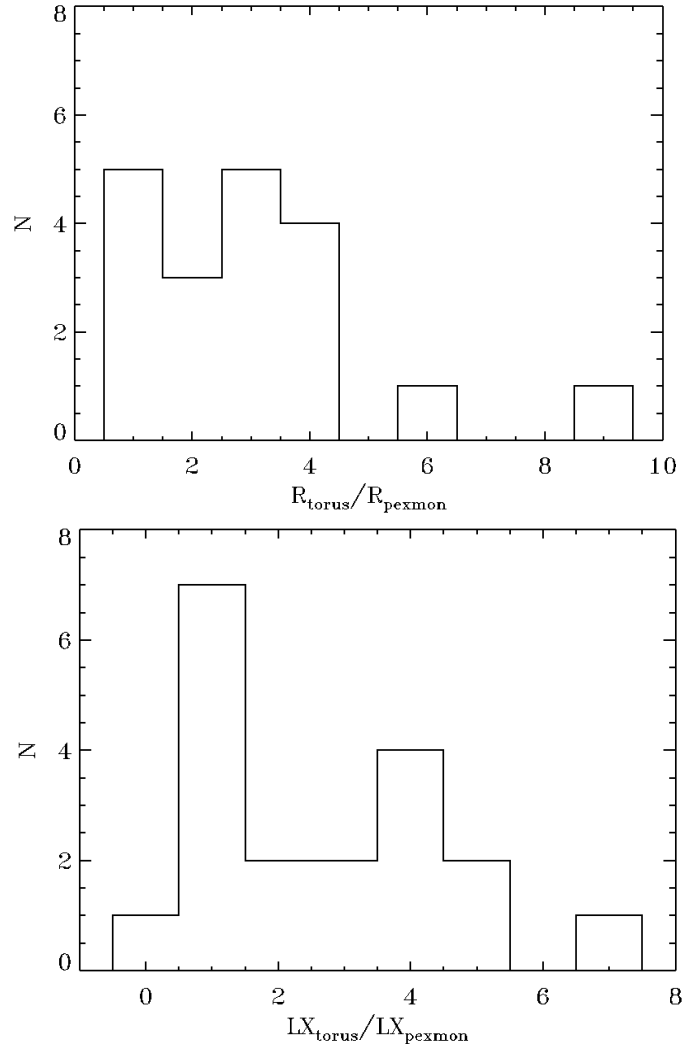


Figure 16. Histograms showing the distribution of (top) the reflection fraction and (bottom) intrinsic 2-10 keV luminosities as determined from the torus model with respect to the pexmon model.

predictions of the same nature as made by Ghisellini et al. (1994), Ikeda et al. (2009) and Murphy & Yaqoob (2009).

We also present flux suppression factors for both spherical and toroidal geometries as a function of N_{H} for different bands and redshifts. These are particularly relevant for AGN surveys that use the X-ray band as they indicate the effectiveness of each band at detecting heavily obscured systems. It is known that even the hardest X-ray energies are affected by extreme obscuration. Here we quantify the flux suppression in these bands, finding that locally, flux suppression reaches a factor of 10 at $N_{\text{H}} = 10^{25} \text{ cm}^{-2}$ for the > 10 keV bands. This may explain the fewer than expected local Compton thick AGN detected in hard X-ray surveys conducted by *Swift/BAT* and *INTEGRAL*. For the > 10 keV X-ray bands, the flux suppression factor is 10 at $\sim 10^{25} \text{ cm}^{-2}$ for all redshifts. This is because at these energies, Compton scattering is the dominant interaction and source of attenuation in the spectrum. The cross section of this interaction is roughly constant as a function of energy and therefore

the effect of redshift is negligible. Flux suppression in the 2-10 keV band reaches 10 at $6 \times 10^{23} \text{ cm}^{-2}$ but this improves as redshift increases, becoming $\sim 10^{25} \text{ cm}^{-2}$ at $z=3$. For the torus geometry, the flux suppression factors behave similarly to the spherical geometry up to $\sim 4 \times 10^{24} \text{ cm}^{-2}$. Here, the flux suppression factors level off due to reflected flux from the inner part of the torus, which remains constant regardless of the line of sight N_{H} . In all cases though, an absorbing column of $N_{\text{H}}=10^{25}$ leaves all X-ray bands severely insensitive to detection of X-ray sources.

Using model spectral data from the torus simulations, we also investigated the difference in the reflection fractions and intrinsic luminosities as determined by using these new torus data, to that derived from fits with the slab model, `pxmon`. Murphy & Yaqoob (2009) find that the reflection fraction is underestimated by a factor of ~ 6 when they compare their torus data to slab data. We also find that the reflection fraction is systematically higher when using the torus model data, by a factor of 3 on average. Though this is not as high as the underestimation presented by Murphy & Yaqoob (2009), the discrepancy is probably due to differing torus geometries, as they use a cylindrical torus geometry which gives varying N_{H} as a function of inclination angle, whereas we use a spherical torus with constant N_{H} . We also find though, that the intrinsic luminosity derived from the slab models are underestimated with respect to the torus model by a factor of 2-3. Additionally, using the torus model, we find that we are unable to constrain the torus geometrical parameters, the opening angle or the inclination angle using the *XMM-Newton* spectral data. Ikeda et al. (2009) also find that it wasn't possible to constrain these parameters with their model, even with spectral data above 10 keV with *Suzaku*

5.2 Properties of the primary X-ray emission from 12 micron selected galaxies

We have presented the properties of the primary X-ray emission of our sample of 12 micron selected galaxies. As our sample is a heterogeneous mix of galaxies, these results reflect the properties of all X-ray sources. We will present results on individual optical classes in paper II. We do however define a subset of unambiguous AGN using their observed 2-10 keV luminosity though this will of course not include AGN with low X-ray luminosity which may be due to significant absorption or being of intrinsic low luminosity.

We find that the mean power-law index is $\langle \Gamma \rangle = 1.90_{-0.07}^{+0.05}$ for the whole sample, with an intrinsic spread of $\sigma = 0.31_{-0.05}^{+0.05}$. The mean is consistent with previous works on predominantly X-ray selected samples. For example Nandra & Pounds (1994) who find $\langle \Gamma \rangle = 1.95 \pm 0.05$ and $\sigma_p = 0.15 \pm 0.04$ for their sample of Seyfert galaxies observed with *Ginga*. We do find a larger intrinsic spread in the indices though than Nandra & Pounds (1994). Our result is also consistent with the results from harder X-ray selected samples (eg. 1.93 for all Seyferts in the *INTEGRAL* catalogue of Beckmann et al. 2009).

Comparing the distribution of power-law indices for obscured sources and unobscured sources is a key test of the unification scheme, which states that the central engine is the same for both, the difference being the orientation of the system to the observer (Antonucci 1993; Urry & Padovani

1995). If a systematic difference is found in these distributions, it would suggest that this is not simply the case. Comparing the average X-ray spectra of Seyfert galaxies with *Ginga* and *OSSE* data, Zdziarski et al. (1995) originally found a systematic difference between the Γ distributions of Seyfert 1s and Seyfert 2s, however, more recent works have tended to find that the distributions are indeed consistent with each other, generally due to the inclusion of more complex spectral models, such as Compton reflection components (e.g. Dadina 2008). We investigated these distributions for obscured and unobscured sources, as well as obscured and unobscured unambiguous AGN. Our analysis showed that the means of these distributions in both cases are not significantly different (the means lie within one sigma of each other) and a K-S test supports the same conclusion, implying that the X-ray generation mechanism in both obscured and unobscured AGN is the same, lending support to AGN unification. The fact that the intrinsic dispersions are similar also supports this conclusion. Beckmann et al. (2009) carried out the same analysis for obscured and unobscured sources on *INTEGRAL* data, which should be less affected by absorption effects, and also find no significant differences between their obscured and unobscured sources. Despite all of this, however, we do notice that the Γ distribution of obscured AGN is skewed towards low Γ values. We discount the possibility of unidentified reflection in these sources, but results presented by Malizia et al. (2003) suggest an alternative cause. They also find a harder distribution of Γ values for Seyfert 2s with respect to Seyfert 1s from their analysis of *Beppo-SAX* data, but reconcile this difference by including more complex absorption models, such as partial covering scenarios, which also improve their fits. There have been several instances where absorption in AGN has been shown to be more complex than a single smooth obscurer, for example NGC 1365, which shows rapid variability in the line of sight obscuration (Risaliti et al. 2009) and further examples by Ricci et al. (2010). As we do not use partial covering models, this may be the reason for the skewed distribution towards low Γ values in our obscured AGN.

We have also investigated any correlation between the power-law index and the intrinsic X-ray luminosity (Fig. 11). Our results don't support a correlation between these two quantities however. This was also found by George et al. (2000) in their sample of local AGN using *ASCA* data. At higher redshifts however, there have been reports of a correlation between Γ and L_X . For example Dai et al. (2004) find an anti-correlation between the two for their mini-survey of $1.7 < z < 4$ sources observed with *XMM-Newton* and *Chandra* in the luminosity range of $10^{43-45} \text{ erg s}^{-1}$. This finding was later supported by Saez et al. (2008) for the *Chandra* deep fields who use a larger range in luminosity ($10^{42-45} \text{ erg s}^{-1}$) and redshift (0.1-4) with 173 AGN. Our luminosity range is $10^{38-44} \text{ erg s}^{-1}$, which is somewhat lower than the higher redshift studies, though the local sample of George et al. (2000) ranges from $10^{42-46} \text{ erg s}^{-1}$, with no correlation. This may suggest an evolutionary effect, or a selection effect in the X-ray samples. Our sample does not suffer from such effects, as it is MIR selected.

5.3 Properties of X-ray obscuration in 12 micron selected galaxies

5.3.1 Compton thick sources

We find that 16/126 ($=13 \pm 3\%$) of the whole sample of sources studied in this sample are Compton thick. For X-ray bright AGN ($L_X > 10^{42}$ ergs $^{-1}$), there are 11/60 ($=18 \pm 5\%$) Compton thick sources. This fraction is important for synthesis models of the XRB and the accretion history of the universe. For X-ray samples selected above 10 keV, the Compton thick fraction has been constrained to be less than that predicted by the XRB. Beckmann et al. (2009) found that only $4 \pm 2\%$ of the AGN in their sample are Compton thick, whereas the XRB predicts a fraction close to 15% at the corresponding limiting flux. Treister et al. (2009) claim that the observed differences between observation and models is due to degeneracies in the parameters of the models, and that only direct observations of Compton thick AGN can determine their relative number. However when accounting for the biases present in hard X-ray selection, Burlon et al. (2010) recover a 20% Compton thick fraction in the *Swift*/*BAT* survey, which is consistent with the XRB and our results.

The Compton thick fraction that we measure in 12 micron selected sources is almost $3\text{-}\sigma$ greater than that measured in hard X-ray selected sources, suggesting that mid-IR selection is more efficient than hard X-ray selection in finding Compton thick AGN. This is explained by the suppression of X-ray flux in the >10 keV bands at high column densities, which we have shown to be a factor >10 at $N_H = 10^{25}$ cm $^{-2}$ using our Monte-Carlo X-ray transmission results.

The XRB synthesis models of Gilli et al. (2007) allow the prediction of the number counts expected from an X-ray survey given the set of parameters of that survey¹. As this sample is not X-ray flux limited, the comparison is not straightforward. However, the Compton thick fraction expected for a survey with our redshift range ($0 < z < 0.1$) and 2-10 keV luminosity range ($10^{42} < L_X < 10^{44}$, a lower limit of $L_X > 10^{42}$ as we are only considering AGN) lies between $\sim 2\%$ and $\sim 20\%$ for X-ray limiting fluxes between $\sim 10^{-13}$ and $\sim 10^{-14}$ ergs cm $^{-2}$ s $^{-1}$, in between which our ‘effective’ X-ray flux limit lies (see Fig. 5). Thus our results would seem roughly consistent with the XRB models.

From the four Compton thick AGN which we manage to measure the N_H directly with **trans**, in three of these cases, a prominent iron line aids in the determination of the N_H . However in the fourth source, NGC 1667, the spectrum does not present an prominent iron line. Here the model is required to fit a hard excess seen in spectrum, but the N_H is not well constrained ($N_H = 271_{-251}^{+5730}$). This is a low signal to noise spectrum, and should be considered a marginal Compton thick source. This technique of fitting hard excesses in Brightman & Nandra (2008), where we show that it can be an effective method of identifying heavily obscured nuclei (e.g. the *Chandra* observation of NGC 4501). In the absence of high signal to noise data around the Fe K α line, or data above 10 keV, this method is the next best thing

for picking out Compton thick candidates from X-ray spectral data alone. This may then motivate longer exposures to gain higher signal to noise data, or observations of broader banded telescopes such as *Suzaku*.

We also infer the Compton thick nature of 12 sources from their reflection dominated spectra, which we define as being those with $R_{\text{pexmon}} > 8$. Though this definition is arbitrary, it is well supported in most sources by high Fe K α EWs or a directly measured $N_H > 10^{24}$ cm $^{-2}$. Lowering this criterion to, e.g. $R_{\text{pexmon}} > 1$ would include two further sources, NGC 4631 and NGC 4666, without prior indications of being heavily absorbed. However, these sources don’t have well constrained Fe K α EWs and hence don’t support a lower R_{pexmon} criterion. If a higher value was chosen, e.g. $R_{\text{pexmon}} > 20$, this would exclude two sources, NGC 1068 and 2MASXJ15504152. However, NGC 1068 is well known to be Compton thick, and as such motivated the criterion in the first place. We therefore conclude that the $R_{\text{pexmon}} > 8$ criterion is best suited to selecting Compton thick AGN.

5.3.2 N_H distribution and obscured fraction

The N_H distribution of AGN has a peak at low column densities, which consists of all unobscured sources. For obscured sources, the distribution peaks in the $N_H = 10^{23-24}$ cm $^{-2}$ bin. We find that 29/60 ($=48 \pm 6\%$) of X-ray luminous AGN are heavily obscured ($N_H \geq 10^{23}$ cm $^{-2}$). Recent studies into the distribution of absorbing columns, such as that by Tueller et al. (2008), reveal that for their sample of *Swift*/*BAT* 14-195 keV selected AGN, $31 \pm 5\%$ are heavily obscured, which is a greater than $3\text{-}\sigma$ difference. Their sample does however extend to higher X-ray luminosities, which will include a greater fraction of unobscured sources due to the dependence they find of obscuration on luminosity. We also intend to investigate the N_H distribution for the AGN in our sample, but using optical line emission to define the AGN in paper II. It is likely here that AGN definition based on X-ray luminosity alone will bias a sample. Those sources which do not meet the luminosity criterion, but have $N_H > 10^{23}$ cm $^{-2}$ are also likely to be AGN.

Our analysis of the dependence of obscuration on luminosity shows that obscuration depends heavily on the intrinsic power of the X-ray source. The data show that obscuration peaks at $L_X = 10^{42}$ ergs $^{-1}$, and declines steeply both above and below this. Several previous studies have reported the decline in the obscured fraction above 10^{42} ergs $^{-1}$ in X-ray selected samples (Ueda et al. 2003; La Franca et al. 2005; Akylas et al. 2006; Tueller et al. 2008; Beckmann et al. 2009), which we confirm here in our MIR selected sample. These results are in support of the ‘receding torus’ model of Lawrence (1991) and Simpson (2005) which describe the decrease in the covering fraction of the torus in AGN with source luminosity, due to sublimation of dust. The decline that we show below 10^{42} ergs $^{-1}$ may be caused in part by the inclusion of non-AGN powered sources which emit at these lower luminosities. However, recently, Burlon et al. (2010) find compelling evidence for a decrease in the obscured fraction at low X-ray luminosities from analysis of the X-ray luminosity functions of obscured and unobscured AGN from the *Swift*/*BAT* survey. Akylas & Georgantopoulos (2009) also evidence for a lower incidence of obscuration at low X-ray luminosities in their optically selected sample.

¹ An online calculator can be found here: <http://www.bo.astro.it/~gilli/counts.html>

Both sets of authors suggest this may be due to the sustenance of torus by accretion driven winds modelled by Elitzur & Shlosman (2006). Our result must be confirmed though with a non-X-ray luminosity dependent method of identifying AGNs, which we intend to do in paper II using optical AGN classifications.

6 CONCLUSIONS

In summary, we have presented an X-ray spectral analysis of the 126 galaxies with *XMM-Newton* coverage in the 12MGS, which is a relatively unbiased and representative selection of galaxies. We have done so with the help of new X-ray radiative transfer calculations, based on Monte-Carlo simulations which take into account photo-electric absorption, Compton scattering and includes fluorescent iron line emission. We have compiled new X-ray spectral models from these data, **trans** and **torus** which we have presented here. These table models are available publicly on the web at

<http://astro.ic.ac.uk/mbrightman/home>

Our main results from these models have been:

- unobscured AGN with a presumed toroidal distribution of matter around it can achieve a maximum iron $K\alpha$ equivalent width of ~ 150 eV, a useful limit to consider when assessing if a source is truly unobscured or not. From our calculations, we show that in order to exceed this EW, the line of sight must be obscured with $N_{\text{H}} > 10^{23} \text{ cm}^{-2}$ (e.g. NGC 3690).

- for $N_{\text{H}} = 10^{25} \text{ cm}^{-2}$, the flux seen in the 10-40 keV, 20-100 keV (*INTEGRAL*), and 14-195 keV (*Swift/BAT*) bands is only 10% of the intrinsic flux, which is important for considering the biases present against hard X-ray selected, heavily obscured AGN. At this N_{H} , 10% or less of the intrinsic flux is seen in any X-ray band at all redshifts, which reveals the bias present in all X-ray surveys against such heavily obscured systems.

- using spectral models based on slab geometries such as **pexrav** or **pexmon** will underestimate the reflection fraction and intrinsic luminosities with respect to toroidal geometries by a factor of 2-3, leading to underestimation of the intrinsic luminosity of the source, as also found by Murphy & Yaqoob (2009).

By combining the positive attributes of 12 micron selection with the penetrative power of X-rays, we have been able to determine the intrinsic X-ray properties of galaxies such as source power, power-law index, and in addition we have assessed the absorption occurring in the sources. We have improved upon previous works on this sample with better signal to noise, spectral resolution and larger band pass by using *XMM-Newton* data. We have developed a detailed systematic approach to the fitting of the spectral data, with the aim of determining the intrinsic power, Γ and N_{H} as accurately as possible. We have paid particular attention to the uncovering of Compton thick sources using our new model, **trans** and the **pexmon** model. The main conclusions from this study have been:

- we find the mean primary power-law index to be $\langle \Gamma \rangle = 1.90^{+0.05}_{-0.07}$ for our sample with an intrinsic spread of $\sigma = 0.31^{+0.05}_{-0.05}$. The index is consistent with previous works,

though we find a larger intrinsic dispersion in our results than previously reported.

- we also find that the mean power-law index for obscured and unobscured sources is consistent with the two source populations being the same, supporting unified schemes.

- we find no dependence of Γ on X-ray luminosity as has been previously reported for local AGN.

- we find an 18% Compton thick fraction for the X-ray AGN defined here, which is higher than the hard X-ray selected samples, but roughly consistent with XRB predictions.

- the obscured fraction for our sample is a strong function of X-ray luminosity, peaking at a luminosity of $\sim 10^{42-43} \text{ erg s}^{-1}$. The decline in the obscured fraction at high luminosities, where these sources are unambiguously AGN, is a confirmation of previous works. The decline at lower luminosities has also been suggested but needs further explanation accounting for optical spectroscopic classifications.

7 ACKNOWLEDGEMENTS

We would like to thank the anonymous referee for the careful reading of this manuscript and the constructive criticism provided. MB would like to thank STFC for financial support. This research has made use of data obtained from the High Energy Astrophysics Science Archive Research Center (HEASARC), provided by NASA's Goddard Space Flight Center. This research has made use of the NASA/IPAC Extragalactic Database (NED) which is operated by the Jet Propulsion Laboratory, California Institute of Technology, under contract with the National Aeronautics and Space Administration. We thank those who built and operate *XMM-Newton*.

REFERENCES

- Akylas A., Georgantopoulos I., 2009, *A&A*, 500, 999
 Akylas A., Georgantopoulos I., Georgakakis A., Kitsionas S., Hatziminaoglou E., 2006, *A&A*, 459, 693
 Anders E., Grevesse N., 1989, *GeCoA*, 53, 197
 Antonucci R., 1993, *ARA&A*, 31, 473
 Awaki H., Koyama K., Inoue H., Halpern J. P., 1991, *PASJ*, 43, 195
 Ballet J., 1999, *A&AS*, 135, 371
 Bambynek W., CRASEMANN B., FINK R. W., FREUND H. U., MARK H., SWIFT C. D., PRICE R. E., RAO P. V., 1972, *Rev. Mod. Phys.*, 44, 716
 Barcons X., Franceschini A., de Zotti G., Danese L., Miyaji T., 1995, *ApJ*, 455, 480
 Beckmann V., Gehrels N., Shrader C. R., Soldi S., 2006, *ApJ*, 638, 642
 Beckmann V., Soldi S., Ricci C., Alfonso-Garzón J., Courvoisier T., Domingo A., Gehrels N., Lubiński P., Mas-Hesse J. M., Zdziarski A. A., 2009, *A&A*, 505, 417
 Brightman M., Nandra K., 2008, *MNRAS*, 390, 1241
 Burlon D., Ajello M., Greiner J., Comastri A., Merloni A., Gehrels N., . 2010, *ArXiv e-prints*
 Dadina M., 2008, *A&A*, 485, 417
 Dai X., Chartas G., Eracleous M., Garmire G. P., 2004, *ApJ*, 605, 45

- Della Ceca R., Ballo L., Tavecchio F., Maraschi L., Petrucci P. O., Bassani L., Cappi M., Dadina M., Franceschini A., Malaguti G., Palumbo G. G. C., Persic M., 2002, *ApJL*, 581, L9
- Elitzur M., Shlosman I., 2006, *ApJL*, 648, L101
- George I. M., Fabian A. C., 1991, *MNRAS*, 249, 352
- George I. M., Turner T. J., Yaqoob T., Netzer H., Laor A., Mushotzky R. F., Nandra K., Takahashi T., 2000, *ApJ*, 531, 52
- Ghisellini G., Haardt F., Matt G., 1994, *MNRAS*, 267, 743
- Gilli R., Comastri A., Hasinger G., 2007, *A&A*, 463, 79
- Guainazzi M., Bianchi S., 2007, *MNRAS*, 374, 1290
- Haardt F., Maraschi L., 1991, *ApJL*, 380, L51
- Horst H., Gandhi P., Smette A., Duschl W. J., 2008, *A&A*, 479, 389
- Ikeda S., Awaki H., Terashima Y., 2009, *ApJ*, 692, 608
- Kallman T. R., Palmeri P., Bautista M. A., Mendoza C., Krolik J. H., 2004, *ApJS*, 155, 675
- Kirsch M. G. F., Altieri B., Chen B., Haberl F., Metcalfe L., Pollock A. M., Read A. M., Saxton R. D., Sembay S., Smith M. J., 2004, in G. Hasinger & M. J. L. Turner ed., *Society of Photo-Optical Instrumentation Engineers (SPIE) Conference Series Vol. 5488 of Society of Photo-Optical Instrumentation Engineers (SPIE) Conference Series, XMM-Newton (cross)-calibration*. pp 103–114
- La Franca F., Fiore F., Comastri A., Perola G. C., Sacchi N., Brusa M., Cocchia F., Feruglio C., Matt G., Vignali C., Carangelo N., Ciliegi P., Lamastra A., Maiolino R., Mignoli M., Molendi S., Puccetti S., 2005, *ApJ*, 635, 864
- Lampton M., Margon B., Bowyer S., 1976, *ApJ*, 208, 177
- Lawrence A., 1991, *MNRAS*, 252, 586
- Longinotti A. L., Cappi M., Nandra K., Dadina M., Pellegrini S., 2003, *A&A*, 410, 471
- Lucy L. B., 2002, *A&A*, 384, 725
- Maccacaro T., Gioia I. M., Wolter A., Zamorani G., Stocke J. T., 1988, *ApJ*, 326, 680
- Magdziarz P., Zdziarski A. A., 1995, *MNRAS*, 273, 837
- Malizia A., Bassani L., Stephen J. B., Di Cocco G., Fiore F., Dean A. J., 2003, *ApJL*, 589, L17
- Matt G., 2002, *MNRAS*, 337, 147
- Matt G., Brandt W. N., Fabian A. C., 1996, *MNRAS*, 280, 823
- Moran E. C., Lehnert M. D., Helfand D. J., 1999, *ApJ*, 526, 649
- Morrison R., McCammon D., 1983, *ApJ*, 270, 119
- Murphy K. D., Yaqoob T., 2009, *MNRAS*, 397, 1549
- Nandra K., George I. M., 1994, *MNRAS*, 267, 974
- Nandra K., O'Neill P. M., George I. M., Reeves J. N., 2007, *MNRAS*, 382, 194
- Nandra K., Pounds K. A., 1994, *MNRAS*, 268, 405
- Piccinotti G., Mushotzky R. F., Boldt E. A., Holt S. S., Marshall F. E., Serlemitsos P. J., Shafer R. A., 1982, *ApJ*, 253, 485
- Pier E. A., Krolik J. H., 1992, *ApJ*, 401, 99
- Ptak A., Serlemitsos P., Yaqoob T., Mushotzky R., 1999, *ApJS*, 120, 179
- Ricci C., Beckmann V., Audard M., Courvoisier T., 2010, *A&A*, 518, A47+
- Risaliti G., Salvati M., Elvis M., Fabbiano G., Baldi A., Bianchi S., Braitto V., Guainazzi M., Matt G., Miniutti G., Reeves J., Soria R., Zezas A., 2009, *MNRAS*, 393, L1
- Rush B., Malkan M. A., Fink H. H., Voges W., 1996, *ApJ*, 471, 190
- Rush B., Malkan M. A., Spinoglio L., 1993, *ApJS*, 89, 1
- Rybicki G. B., Lightman A. P., 1986, *Radiative Processes in Astrophysics*. *Radiative Processes in Astrophysics*, by George B. Rybicki, Alan P. Lightman, pp. 400. ISBN 0-471-82759-2. Wiley-VCH, June 1986.
- Saez C., Chartas G., Brandt W. N., Lehmer B. D., Bauer F. E., Dai X., Garmire G. P., 2008, *AJ*, 135, 1505
- Simpson C., 2005, *MNRAS*, 360, 565
- Smith R. K., Brickhouse N. S., Liedahl D. A., Raymond J. C., 2001, *ApJL*, 556, L91
- Sobolewska M. A., Done C., 2007, *MNRAS*, 374, 150
- Spinoglio L., Malkan M. A., 1989, *ApJ*, 342, 83
- Spinoglio L., Malkan M. A., Rush B., Carrasco L., Recillas-Cruz E., 1995, *ApJ*, 453, 616
- Sunyaev R. A., Titarchuk L. G., 1980, *A&A*, 86, 121
- Treister E., Urry C. M., Virani S., 2009, *ApJ*, 696, 110
- Tueller J., Baumgartner W. H., Markwardt C. B., Skinner G. K., Mushotzky R. F. e. a., 2010, *ApJS*, 186, 378
- Tueller J., Mushotzky R. F., Barthelmy S., Cannizzo J. K., Gehrels N., Markwardt C. B., Skinner G. K., Winter L. M., 2008, *ApJ*, 681, 113
- Turner T. J., George I. M., Nandra K., Mushotzky R. F., 1997, *ApJS*, 113, 23
- Turner T. J., Pounds K. A., 1989, *MNRAS*, 240, 833
- Ueda Y., Akiyama M., Ohta K., Miyaji T., 2003, *ApJ*, 598, 886
- Urry C. M., Padovani P., 1995, *PASP*, 107, 803
- Verner D. A., Ferland G. J., Korista K. T., Yakovlev D. G., 1996, *ApJ*, 465, 487
- Yaqoob T., 1997, *ApJ*, 479, 184
- Yaqoob T., Murphy K. D., 2010, *ArXiv e-prints*
- Zdziarski A. A., Johnson W. N., Done C., Smith D., McNaron-Brown K., 1995, *ApJL*, 438, L63

Table 2: Observational data for the 126 XMM-Newton observations used here. Col. (1) Galaxy name as given by NED; Col. (2) Galaxy name as given by Rush et al. (1993); Col. (3) Right ascension in decimal J2000 co-ordinates (RMS); Col. (4) Declination in decimal J2000 co-ordinates (RMS); Col. (5) Redshift as reported in NED. * Messier 81, NGC 4214 and Messier 90 have reported negative redshifts, indicating that they have peculiar velocities in our direction. We use the luminosity distance reported in NED when calculating the luminosities for these objects (0.662, 7.54 and 1.22 Mpc respectively); Col. (6) XMM-Newton observation identifier; Col. (7) XMM-Newton revolution number; Col. (8) Date of XMM-Newton observation; Col. (9) Duration of the XMM-Newton observation before background screening (ks); Col. (10) Exposure time after screening and dead-time correction; Col. (11) XMM-Newton readout mode. FW = full window, FWe = full window extended, LW = large window, SW = small window; Column (12) Optical filter in place during XMM-Newton observation.

Name (NED) (1)	Name (RMS) (2)	RA (J2000) (3)	Dec. (J2000) (4)	z (5)	Obs ID (6)	Rev (7)	Date (8)	Duration (9)	Exposure (10)	Mode (11)	Filter (12)
MRK 0335	MRK335	1.576	20.201	0.0258	306870101	1112	2006-01-03	133.3	82.5	SW	Thin
NGC 0017	N34=MK938	2.778	-12.107	0.0196	150480501	556	2002-12-22	22.2	10.9	FW	Medium
NGC 0150	N150	8.567	-27.803	0.0053	44350101	452	2002-05-29	22.9	11.9	FW	Medium
NGC 0214	N214	10.367	25.499	0.0151	153030101	653	2003-07-04	15.9	8.1	FW	Thin
NGC 0262	N262=MK348	12.201	31.957	0.0150	67540201	477	2002-07-18	49.5	21	FW	Medium
UGC 00545	IZW1	13.405	12.697	0.0611	300470101	1027	2005-07-18	85.5	50.8	SW	Medium
NGC 0424	N424=TOL0109	17.862	-38.085	0.0118	2942301	367	2001-12-10	8.2	4.5	FW	Medium
NGC 0526A	N526A	20.978	-35.065	0.0191	150940101	647	2003-06-21	47.9	37.5	LW	Thin
NGC 0513	N513	21.114	33.800	0.0195	301150401	1124	2006-01-28	16.9	8.9	FW	Thin
NGC 0520	N520	21.143	3.791	0.0076	25541601	378	2002-01-01	13.1	8.9	FW	Medium
NGC 0660	N660	25.759	13.646	0.0028	93641001	198	2001-01-07	12.2	6.3	FWe	Medium
2MASX_J01500266-0725482	F01475-0740	27.515	-7.428	0.0177	200431101	754	2004-01-21	11.9	9	FW	Thin
NGC 0695	N695	27.808	22.582	0.0325	204410101	751	2004-01-14	11.9	2.4	FW	Medium
NGC 1052	N1052	40.263	-8.257	0.0050	306230101	1116	2006-01-12	54.9	46.9	FW	Medium
MESSIER 077	N1068	40.672	-0.013	0.0038	111200101	117	2000-07-29	42.3	33.1	LW	Medium
ARP 118	N1143/4	43.803	-0.183	0.0288	312190401	1124	2006-01-28	11.9	8.9	FW	Thin
MCG -02-08-039	M-2-8-39	45.129	-11.415	0.0299	301150201	1112	2006-01-23	23.4	7	FW	Thin
NGC 1194	N1194	45.952	-1.104	0.0136	307000701	1135	2006-02-19	16.1	12.4	FW	Medium
NGC 1291	N1291	49.327	-41.108	0.0028	201690201	929	2005-01-03	34.9	18.7	FW	Medium
NGC 1313	N1313	49.570	-66.492	0.0016	405090101	1255	2006-10-16	123.2	91.6	FW	Medium
NGC 1316	N1316	50.672	-37.209	0.0059	302780101	1039	2005-08-11	107.6	76.8	FWe	Thin
NGC 1320	N1320=MK607	51.200	-3.043	0.0089	405240201	1219	2006-08-06	17.1	12.5	FW	Thin
NGC 1365	N1365	53.402	-36.140	0.0055	205590301	752	2004-01-17	59.7	51.2	FW	Medium
NGC 1386	N1386	54.190	-6.320	0.0029	140950201	560	2002-12-29	17.4	13.8	FW	Medium
NGC 1482	N1482	58.666	-20.502	0.0064	150910101	583	2003-02-14	18.9	7.4	FW	Medium
3C 120	3C120	68.294	5.355	0.0330	152840101	680	2003-08-26	133.9	78.5	SW	Medium
NGC 1614	N1614	68.501	-8.579	0.0159	150480201	583	2003-02-13	23.9	15.7	FW	Medium
MRK 0618	MRK618	69.097	-10.375	0.0356	307001301	1133	2006-02-15	18.1	6.9	FW	Medium
NGC 1672	N1672	71.428	-59.247	0.0044	203880101	910	2004-11-27	49.9	42.6	FW	Medium
NGC 1667	N1667	72.157	-6.320	0.0152	200660401	876	2004-09-20	10.4	7.4	LW	Thick
NGC 1808	N1808	76.926	-37.514	0.0033	110980801	426	2002-04-06	43.6	31.3	FWe	Thin
ESO 362-G 018	M-5-13-17	79.903	-32.658	0.0124	312190701	1124	2006-01-28	11.9	8.9	FW	Thin
2MASX_J05210136-2521450	F05189-2524	80.256	-25.363	0.0426	85640101	233	2001-03-17	12.3	7	FW	Thin
2MASX_J05580206-3820043	F05563-3820	89.512	-38.335	0.0339	109131001	508	2002-09-17	9.1	3.3	LW	Thin
IC 0450	MRK6	103.055	74.427	0.0188	61540101	238	2001-03-27	46.5	17.6	FW	Medium
UGC 03973	MRK79	115.633	49.810	0.0222	103862101	253	2001-04-26	6.5	3.6	SW	Medium
IRASF07599+6508	F07599+6508	121.138	64.997	0.1488	94400301	344	2001-10-25	23.2	17.3	FW	Medium
NGC 2639	N2639	130.913	50.205	0.0111	301651101	973	2005-04-02	26.1	2.2	FW	Thin
NGC 2655	N2655	133.911	78.224	0.0047	301650301	1051	2005-09-04	11.8	3.6	FW	Thin
IC 2431	I2431=U4756	136.147	14.594	0.0499	303562101	1091	2005-11-24	6.8	4.3	FW	Thin
MRK 0704	MRK704	139.607	16.307	0.0292	300240101	1074	2005-10-21	21.7	12.5	SW	Medium
NGC 2841	N2841	140.516	50.972	0.0021	201440101	901	2004-11-09	41.9	23.7	FW	Thin
UGC 05101	U5101	143.953	61.356	0.0394	85640201	353	2001-11-12	35	26.1	FWe	Thin
NGC 2992	N2992	146.418	-14.323	0.0077	147920301	630	2003-05-19	28.9	21.8	FW	Medium
MESSIER 081	N3034=M81	148.890	69.066	-0.0001*	111800101	251	2001-04-22	132.7	79.7	SW	Medium
MESSIER 082	N3034=M82	148.971	69.678	0.0007	206080101	800	2004-04-21	104.4	63.3	FW	Medium
NGC 3079	N3079	150.491	55.681	0.0037	110930201	246	2001-04-13	25.3	13.6	FWe	Thin
NGC 3147	N3147	154.231	73.398	0.0094	405020601	1250	2006-10-06	17.2	13.6	LW	Thin
NGC 3227	N3227	155.881	19.864	0.0039	101040301	178	2000-11-28	40.1	30.3	FW	Medium
NGC 3310	N3310	159.693	53.502	0.0033	112840301	260	2001-05-11	19.8	2.7	FW	Thin

NGC 3486	N3486	165.099	28.977	0.0023	112550101	259	2001-05-09	15.2	3.7	FWe	Medium
NGC 3516	N3516	166.703	72.567	0.0088	107460701	352	2001-11-09	130	80.6	SW	Thin
MESSIER 066	N3627	170.064	12.992	0.0024	93641101	268	2001-05-26	11.2	5.3	FWe	Medium
NGC 3690	N3690=MK171	172.136	58.561	0.0104	112810101	258	2001-05-07	22.2	14.6	FW	Thin
NGC 3735	N3735	173.989	70.536	0.0090	301650501	1062	2005-09-27	16.7	0.4	FW	Thin
NGC 3976	N3976	178.991	6.748	0.0083	301651801	1194	2006-06-16	14.4	4.4	FW	Thin
NGC 3982	N3982	179.114	55.127	0.0037	204651201	827	2004-06-15	11.9	9.1	LW	Thin
NGC 4013	N4013	179.631	43.948	0.0028	306060201	1086	2005-11-13	157.2	49.7	FW	Medium
ARP 244	N4038/9	180.480	-18.879	0.0057	85220201	382	2002-01-08	52.8	34.9	FWe	Medium
NGC 4051	N4051	180.791	44.531	0.0023	157560101	541	2002-11-22	51.9	44	LW	Medium
NGC 4151	N4151	182.644	39.402	0.0033	112830201	190	2000-12-22	62.2	50.9	FW	Medium
NGC 4214	N4214	183.917	36.324	-0.0003*	35940201	358	2001-11-22	20.3	12.9	FW	Medium
NGC 4253	MK766	184.608	29.814	0.0129	109141301	265	2001-05-20	129.9	72.2	SW	Medium
MESSIER 099	N4254	184.713	14.414	0.0080	147610101	651	2003-06-29	51	12.8	FWe	Thin
MESSIER 100	N4321	185.724	15.823	0.0052	106860201	376	2001-12-28	36.6	20.6	FWe	Medium
NGC 4388	N4388	186.441	12.664	0.0084	110930701	551	2002-12-12	12	7.3	FWe	Thin
NGC 4414	N4414	186.612	31.223	0.0024	402830101	1200	2006-06-29	42.2	17.8	FW	Thin
NGC 4449	N4449	187.034	44.099	0.0007	112521601	450	2002-05-25	24	1.9	FW	Thin
3C 273	3C273	187.282	2.051	0.1583	136550101	277	2001-06-13	89.8	61.4	SW	Medium
NGC 4490	N4490	187.646	41.647	0.0019	112280201	451	2002-05-27	18.1	11.5	FWe	Medium
MESSIER 088	N4501	187.990	14.422	0.0076	112550801	364	2001-12-04	14	2.5	FWe	Medium
NGC 4559	N4559	188.987	27.960	0.0027	152170501	634	2003-05-27	42.2	34.1	FW	Medium
MESSIER 090	N4569=M90	189.212	13.162	-0.0008*	200650101	918	2004-12-13	66	44.2	FWe	Thin
MESSIER 058	N4579	189.428	11.820	0.0051	112840101	642	2003-06-12	23.7	15.2	FW	Thin
NGC 4593	N4593	189.917	-5.346	0.0090	109970101	103	2000-07-02	28.1	5	SW	Thin
MESSIER 104	N4594	190.001	-11.624	0.0005	84030101	376	2001-12-28	86.9	15.6	FWe	Thin
NGC 4631	N4631	190.529	32.543	0.0020	110900201	467	2002-06-28	54.8	36.9	FWe	Thin
NGC 4666	N4666	191.282	-0.461	0.0051	110980201	467	2002-06-27	58.2	48	FWe	Thin
NGC 4725	N4725	192.574	25.489	0.0040	112550401	460	2002-06-14	18.6	12.1	FWe	Medium
UGC 08058	MK23=U8058	194.063	56.871	0.0422	81340201	274	2001-06-07	22.3	17.3	FW	Medium
NGC 4968	N4968	196.774	-23.677	0.0099	200660201	837	2004-07-05	17.7	4.8	LW	Thick
NGC 5005	N5005	197.732	37.059	0.0032	110930501	551	2002-12-13	13.6	8.6	FWe	Thin
MESSIER 063	N5055	198.956	42.028	0.0017	405080301	1367	2007-05-28	51.8	7.1	FW	Thin
MCG -03-34-064	M-3-34-63	200.598	-16.726	0.0165	206580101	939	2005-01-24	44.9	35	FW	Medium
NGC 5170	N5170	202.460	-17.972	0.0050	206300101	757	2004-01-27	31.9	17.6	FW	Thin
NGC 5194	N5194=M51	202.473	47.195	0.0015	112840201	568	2003-01-15	20.5	17.2	FW	Thin
ESO 383- G 035	M-6-30-15	203.977	-34.297	0.0077	29740801	303	2001-08-04	130.5	83.4	SW	Medium
MESSIER 083	N5236=M83	204.245	-29.863	0.0017	110910201	574	2003-01-27	30.7	22.4	FWe	Thin
IRAS F13349+2438	F13349+2438	204.325	24.386	0.1076	96010101	97	2000-06-20	130.4	28.5	SW	Thin
NGC 5256 (S)	N5256=MK266	204.576	48.275	0.0279	55990501	445	2002-05-15	23.1	14.2	FWe	Thin
NGC 5253	N5253	204.980	-31.639	0.0014	35940301	305	2001-08-08	47	27.5	FWe	Thin
MRK 0273	MK273=U8696	206.174	55.887	0.0378	101640401	441	2002-05-07	22.8	17.9	FW	Thick
IC 4329A	I4329A	207.331	-30.310	0.0161	147440101	670	2003-08-06	136	68	SW	Thin
UGC 08850 (E)	MK463	209.011	18.372	0.0504	94401201	373	2001-12-22	26.8	21	FW	Medium
NGC 5506	N5506	213.309	-3.207	0.0062	300240201	840	2004-07-11	21.6	14.6	SW	Medium
NGC 5548	N5548	214.499	25.137	0.0172	89960301	290	2001-07-09	95.8	46.7	SW	Thin
NGC 5775	N5775	223.492	3.542	0.0056	150350101	665	2003-07-28	47.2	22.4	FW	Thin
VV 705	IZW107	229.998	-21.317	0.0446	300240201	1031	2005-07-26	23	7.6	LW	Medium
UGC 09944	U9944	229.528	42.745	0.0402	203390601	864	2004-08-28	25.2	9.1	FW	Medium
2MASX J15504152-0353175	F15480-0344	233.950	73.451	0.0245	307002401	1014	2005-06-23	16.1	10.8	FW	Medium
NGC 6240	N6240	237.671	-3.889	0.0303	138951501	667	2003-07-31	12.4	1.5	FW	Medium
NGC 6286	N6286	253.244	2.401	0.0245	101640101	144	2000-09-22	30.1	12.5	FW	Medium
NGC 6552	N6552	254.629	58.939	0.0183	203390701	765	2004-02-12	41.6	1.8	FW	Medium
AM 1925-724	F19254-7245	292.844	-72.656	0.0617	81341001	239	2001-03-30	23.2	13	FW	Thin
NGC 6810	N6810	295.890	-58.656	0.0068	205220101	802	2004-04-25	48.7	31	FW	Medium
NGC 6890	N6890	304.577	-44.806	0.0081	301151001	1063	2005-09-29	12.8	1.2	FW	Thin
MRK 0509	MK509	311.037	-10.724	0.0344	306090201	1073	2005-10-18	86	58.1	SW	Thin
ESO 286-IG 019	E286-IG19	314.614	-42.649	0.0430	81340401	250	2001-04-21	21.7	10	FW	Thin
NGC 7090	N7090	324.118	-54.558	0.0028	200230101	793	2004-04-08	28	3.9	FWe	Thin
NGC 7172	N7172	330.509	-31.869	0.0087	202860101	902	2004-11-11	58.9	40	LW	Thin
NGC 7213	N7213	332.319	-47.166	0.0058	111810101	269	2001-05-29	49.6	29.3	SW	Medium

IC 5169	I5169	332.541	-36.089	0.0104	307002001	1167	2006-04-23	18.6	0.9	FW	Medium
NGC 7252	N7252	335.189	-24.677	0.0160	49340201	354	2001-11-13	28.2	21.2	FW	Medium
3C 445	3C445	335.955	-2.104	0.0562	90050601	365	2001-12-06	23.9	15.1	SW	Thin
NGC 7314	N7314	338.941	-26.050	0.0048	111790101	256	2001-05-02	44.7	26.7	SW	Medium
MCG -03-58-007	M-3-58-7	342.410	-19.272	0.0315	301150301	992	2005-05-09	15.2	2.7	FW	Thin
NGC 7469	N7469	345.815	8.874	0.0163	207090101	912	2004-11-30	85	57.8	SW	Medium
NGC 7479	N7479	346.240	12.325	0.0079	25541001	280	2001-06-19	13.1	6.1	FW	Medium
ESO 148-IG 002	E148-IG02	348.944	-59.054	0.0446	81340301	539	2002-11-19	23.4	8.8	FW	Medium
NGC 7552	N7552	349.040	-42.586	0.0054	93640701	270	2001-05-30	20.6	1.5	FW ^e	Medium
NGC 7582	N7582	349.593	-42.372	0.0053	204610101	987	2005-04-29	101.9	65.6	FW	Medium
NGC 7674	N7674	351.987	8.779	0.0289	200660101	821	2004-06-02	10.4	7.6	LW	Thick
NGC 7714	N7714	354.059	2.155	0.0093	112521301	457	2002-06-07	22.2	13.8	FW	Medium
NGC 7771	N7771	357.853	20.111	0.0143	93190301	464	2002-06-21	32.1	26.8	FW	Medium
MRK 0331	MK331	357.859	20.586	0.0185	203390801	827	2004-06-15	18.4	12.2	FW	Medium

Table 3: Parameters of the basic model consisting of the primary power-law and the thermal plasma component, where present. More complex model parameters are presented in Tables 4 to 8. Column (1) Galaxy name; Column (2) χ^2/DOF of the fit. $(^F)$ indicates that the full band spectral fit method was used, $(^D)$ indicates that although the χ^2 of this fit is bad ($\chi^2_r > 2$), the data/model ratio never exceeded 5%, which is the level of uncertainties in the *XMM-Newton* calibration, $(^H)$ indicates that only the 2.5-10 keV fit parameters have been presented here due to spectral complexities below 2 keV. For the 2.5-10 keV fits, only NGC 1068, NGC 1365 and M82 have bad fits. These sources have notoriously complex spectra, which are high signal to noise in this case, with several emission and absorption features. We do not attempt to fit these additional complexities, however, and present only the basic hard band parameters for these fits. No errors are quoted because the standard formalism does not apply unless the model fits the data (Lampton et al. 1976). ; Column (3) Galactic column density (10^{20} cm^{-2}); Column (4) the neutral column density measured in the primary power-law (10^{22} cm^{-2}). * indicates that an ionised absorber has been detected in this spectral fit, details of which are in Table 7; Column (5) The power-law index of the primary power-law. † indicates that this parameter was fixed in the fit; Column (6) The normalisation of the primary power-law ($\times 10^{-5}$ Photons $\text{cm}^{-2} \text{s}^{-1} \text{keV}^{-1}$ at 1 keV) Column (7) the temperature, in keV, of the thermal plasma component; Column (8) The ratio of the normalisation of the thermal plasma component to the normalisation of the primary power-law. (9) Observed flux in the 2-10 keV band in units of $10^{-14} \text{ ergs s}^{-1} \text{ cm}^{-2}$ and the logarithm of the intrinsic luminosity in this band in units of ergs s^{-1} .

Name (1)	χ^2/DOF (2)	$N_{\text{H}}(\text{Gal})$ (3)	N_{H} (4)	Γ_1 (5)	A_{pl} (6)	kT^{therm} (7)	R^{therm} (8)	$F_{\text{HX}}/L_{\text{HX}}$ (9)
MRK0335	1758.79/143 ^(D)	3.6	- *	2.03 +0.02 -0.02	704 +20 -19	0.27	0.22	1869/43.5
NGC0017	35.15/39	2.1	47.0 +30.4 -21.2	1.9†	36.6 +33.1 -15.9	0.70 +0.11 -0.10	0.0271 +0.0285 -0.0093	28/42.0
NGC0150	76.04/61	1.5	-	1.73 +0.3 -0.3	9.11 +4.40 -5.73	0.35 +0.05 -0.05	0.274 +0.025 -0.0424	38/40.4
NGC0214	6.02/6	3.8	17.3 +13.1 -8.0	1.9†	9.84 +5.73 -3.91	0.35 +0.35 -0.05	0.0507 +0.0374 -0.0082	15/41.2
NGC0262	210.06/140	5.8	13.1 +0.7 -1.3	1.68 +0.07 -0.1	1020 +329 -15	0.20 +0.05 -0.05	0.0016 +0.0007 -0.0007	2809/43.3
UGC00545	79.64/97 ^(H)	4.8	-	2.16 +0.05 -0.04	239 +12 -12	-	-	494/43.6
NGC0424	63.56/46	1.5	23.6 +44.7 -15.8	1.9†	36.7 +822 -27.3	0.74 +0.18 -0.11	0.0514 +0.0593 -0.0279	135/42.5
NGC0526A	179.09/149	2.3	1.14 +0.26 -0.26	1.51 +0.05 -0.05	432 +38 -35	1.2 +0.2	0.0082 +0.0087 -0.0036	2255/43.3
NGC0513	86.71/123	5.2	6.82 +1.60 -1.55	1.69 +0.2 -0.2	128. +70.2 -45.2	0.30 +0.09 -0.13	0.0239 +0.0345 -0.0107	406/42.7
NGC0520	23.05/24	3.1	- *	1.9†	2.25 +0.87 -0.37	0.71 +0.13 -0.13	0.347 +0.365 -0.316	6/40.0
NGC0660	20.3/22	4.7	0.261 +0.146 -0.078	1.9†	4.95 +1.27 -1.15	0.62 +0.73 -0.12	0.303 +0.098 -0.098	15/39.4
2MASXJ01500266	81.95/75	2	0.211 +0.055 -0.006	2.19 +0.3 -0.2	40.1 +17.2 -11.5	-	-	78/41.7
NGC0695	3.89/8	6.9	- *	1.9†	5.67 +2.29 -2.29	0.68 +0.12 -0.21	0.357 +0.395 -0.164	16/41.6
NGC1052	169.33/139	2.8	30.6 +11.4 -26.3	1.72 +0.1 -0.2	142 +64 -67	0.61 +0.04 -0.04	0.0183 +0.0184 -0.0021	465/41.5
NGC1068	235.38/97	3	-	1.84	74	-	-	497/42.2
ARP118	80.27/85	5.9	64.7 +7.8 -6.9	1.9†	545 +79 -67	0.60 +0.17 -0.49	0.0033 +0.073 -0.0022	331/43.6
MCG-02-08-039	64.24/44	5.1	46.9 +13.1 -11.9	1.9†	138 +34 -36	0.19 +0.03 -0.02	1.49 +0.153 -0.20178	83/42.9
NGC1194	55.18/57	6.5	67.8 +18.3 -16.4	1.9†	168 +71 -84	0.76 +0.18 -0.03	0.0671 +0.0459 -0.0681	101/42.3
NGC1291	93.19/66	1.6	- *	2.21 +0.3 -0.3	13.6 +4.8 -4.8	0.38 +0.03 -0.04	0.466 +0.190 +0.089	25/39.7
NGC1313	154.82/133	4	0.151 +0.013 -0.012	1.9†	11.0 +0.3 -0.3	0.26 +0.02 -0.02	0.262 -0.081	37/39.3
NGC1316	83.29/77 ^(H)	2.4	-	2.12 +0.2 -0.2	12.2 +3.0 -2.5	-	-	28/40.3
NGC1320	84.61/53	3.7	204 +91 -99	1.9†	854 +1490 -708	0.82 +0.08 -0.08	0.0029 +0.0030 -0.0008	48/42.7
NGC1365	830.55/95	1.3	17.51	2.81	5271	-	-	1296/42.5
NGC1386	96.32/50	1.3	0.0459 +0.0161 -0.0137	3.35 +0.2 -0.2	7.03 +0.84 -0.77	0.73 +0.04 -0.05	0.523 +0.124 -0.0954	32/40.9
NGC1482	56.64/50 ^(F)	3.4	8.68 +7.19 -3.86	1.93 +0.5 -0.5	21.5 +42.0 -19.1	0.66 +0.04 -0.05	0.183 +0.359 -0.140	59/40.7
3C120	416.19/145 ^(D)	10.6	-	1.75 +0.02 -0.02	1170 +22 -22	0.09	2.37	4569/44.2

Name (1)	χ^2/DOF (2)	N_{Gal} (3)	$N_{\text{H},1}$ (4)	Γ_1 (5)	norm (6)	kT_{therm} (7)	R_{therm} (8)	$F_{\text{HX}}/L_{\text{HX}}$ (9)
NGC1614	67.43/67	6.4	0.194 ^{+0.036} _{-0.027}	2.06 ^{+0.4} _{-0.4}	11.1 ^{+7.8} _{-4.4}	0.75 ^{+0.06} _{-0.04}	0.238 ^{+0.242} _{-0.044}	26/41.2
MRK0618	142.92/127	4.8	- *	2.08 ^{+0.1} _{-0.08}	390 ⁺⁵¹ ₋₁₀	0.070 ^{+0.13} _{-0.070}	1.45 ^{+9.59} _{-1.45}	940/43.4
NGC1672	117.82/63	1.7	0.0304 ^{+0.009} _{-0.007}	1.82 ^{+0.2} _{-0.3}	2.36 ^{+1.10} _{-0.82}	0.62 ^{+0.02} _{-0.02}	16.4 ^{+8.2} _{-8.2}	9/39.6
NGC1667	17.67/15 ^(F)	5.4	271 ⁺⁵⁷³⁰ ₋₂₅₁	1.9 [†]	370 ⁺⁶²¹⁰⁰ ₋₃₇₀	0.30 ^{+0.02} _{-0.02}	0.0062 ^{+1.04} _{-1.06}	10/42.8
NGC1808	229.82/123	2.5	8.73 ^{+6.82} _{-7.56}	1.39 ^{+0.4} _{-0.3}	10.0 ^{+16.0} _{-6.9}	0.66 ^{+0.02} _{-0.02}	15.0 ^{+15.2} _{-2.1}	102/40.4
ESO362-G018	165.27/124	1.8	15.6 ^{+8.1} _{-9.7} *	1.53 ^{+0.4} _{-0.2}	67.5 ^{+11.4} _{-26.0}	0.10 ^{+0.01} _{-0.01}	0.614 ^{+0.633} _{-0.153}	335/42.4
2MASXJ05210136	96.92/101 ^(F)	1.7	6.58 ^{+0.88} _{-0.76}	2.08 ^{+0.2} _{-0.06}	199 ⁺⁷⁴ ₋₆₁	-	-	315/44.2
2MASXJ05580206	93.48/100 ^(H)	3.9	-	1.67 ^{+0.04} _{-0.05}	1040 ⁺⁶⁹ ₋₆₉	-	-	4226/44.1
IC0450	186.44/137	5.5	2.91 ^{+0.79} _{-0.22} *	1.50 ^{+0.09} _{-0.09}	219 ⁺¹⁶ ₋₃₄	-	-	1258/43.1
UGC03973	134.41/127	5.3	- *	1.57 ^{+0.09} _{-0.08}	233 ⁺³² ₋₂₆	0.20 ^{+0.02} _{-0.03}	0.646 ^{+0.647} _{-0.303}	1212/43.8
IRAS F07599+6508	38.26/28	4.2	-	1.9 [†]	0.726 ^{+0.005} _{-0.005}	-	-	2/42.1
NGC2639	65.5/51	3	-	1.9 [†]	1.56 ^{+6.55} _{-1.56}	0.59 ^{+0.13} _{-0.16}	2.74 ^{+2.80} _{-0.80}	5/40.1
NGC2655	40.84/35	2.1	23.0 ^{+9.5} _{-5.3}	1.9 [†]	100 ⁺²⁷ ₋₂₁	0.61 ^{+0.06} _{-0.06}	0.0647 ^{+0.067} _{-0.011}	105/41.7
IC2431	11.69/16 ^(F)	3.7	< 0.04	1.9 [†]	1.32 ^{+0.51} _{-0.43}	0.81 ^{+0.06} _{-0.11}	1.94 ^{+0.97} _{-0.88}	4/41.4
MRK0704	251.24/141	3	1.62 ^{+0.83} _{-0.09} *	1.73 ^{+0.2} _{-0.1}	311 ⁺⁸¹ ₋₆₁	-	-	1025/43.4
NGC2841	104.63/79	1.4	-	1.9 [†]	5.45 ^{+0.74} _{-0.74}	0.48 ^{+0.11} _{-0.16}	0.230 ^{+0.253} _{-0.051}	16/39.2
UGC05101	43.8/51	3	49.6 ^{+25.4} _{-18.2}	1.9 [†]	25.8 ^{+17.4} _{-10.3}	0.78 ^{+0.28} _{-0.21}	0.0196 ^{+0.0261} _{-0.0108}	18/42.5
NGC2992	110.95/92 ^(H)	4.8	0.407 ^{+0.165} _{-0.165}	1.59 ^{+0.03} _{-0.03}	1770 ⁺⁹⁶ ₋₉₆	-	-	8422/43.1
MESSIER081	219.32/145	5.1	-	1.83 ^{+0.03} _{-0.02}	319 ⁺¹⁰ ₋₈₄	0.94 ^{+0.09} _{-0.15}	0.0244 ^{+0.0252} _{-0.0079}	1115/38.8
MESSIER082	286.58/92	5.1	-	1.74	31	-	-	1205/40.1
NGC3079	89.37/69	8.6	0.0532 ^{+0.049} _{-0.041}	2.42 ^{+0.3} _{-0.2}	9.56 ^{+2.58} _{-1.93}	0.73 ^{+0.05} _{-0.10}	0.482 ^{+0.126} _{-0.126}	34/40.9
NGC3147	118.87/115	2.9	0.0133 ^{+0.004} _{-0.004}	1.52 ^{+0.2} _{-0.1}	25.3 ^{+6.6} _{-4.9}	1.2 ^{+0.0} _{-0.5}	0.0915 ^{+0.097} _{-0.050}	141/41.4
NGC3227	193.85/137	2.2	7.93 ^{+2.08} _{-2.14} *	1.54 ^{+0.03} _{-0.00}	193 ⁺¹¹ ₋₆	0.26 ^{+0.01} _{-0.01}	0.154 ^{+0.0428} _{-0.027}	883/41.6
NGC3310	85.72/45 ^(F)	1.3	0.0700 ^{+0.0202} _{-0.0163}	1.93 ^{+0.1} _{-0.1}	30.4 ^{+4.0} _{-3.5}	0.67 ^{+0.07} _{-0.07}	0.169 ^{+0.072} _{-0.050}	87/40.3
NGC3486	33.92/22	1.9	-	1.9 [†]	3.32 ^{+2.01} _{-2.01}	-	-	10/39.9
NGC3516	92.03/96 ^(H)	3.4	32.7 ^{+3.9} _{-3.9}	2.03 ^{+0.09} _{-0.07}	794 ⁺²⁴³ ₋₁₇₁	-	-	1563/43.8
MESSIER066	32.2/29	2.1	- *	1.9 [†]	8.05 ^{+1.44} _{-1.44}	0.63 ^{+0.10} _{-0.08}	0.951 ^{+1.31} _{-0.682}	23/39.5
NGC3690	128.81/93	0.9	0.0614 ^{+0.0557} _{-0.0614}	1.88 ^{+0.2} _{-0.2}	24.3 ^{+7.6} _{-5.8}	0.72 ^{+0.03} _{-0.03}	0.655 ^{+0.683} _{-0.066}	83/41.3
NGC3735	34.98/43 ^(F)	1.2	0.0270 ^{+0.0641} _{-0.0270}	1.9 [†]	3.11 ^{+1.57} _{-1.39}	-	-	9/40.2
NGC3976	27.96/33	1.1	- *	1.9 [†]	2.58 ^{+1.20} _{-1.20}	0.52 ^{+0.10} _{-0.13}	0.354 ^{+0.390} _{-0.151}	7/40.1
NGC3982	60.97/29	1	21.7	1.83	13	0.31	0.24	19/40.2
NGC4013	47.23/41	1.3	8.86 ^{+6.18} _{-4.44} *	1.9 [†]	1.97 ^{+0.87} _{-0.69}	0.22 ^{+0.05} _{-0.04}	0.164 ^{+0.226} _{-0.071}	4/39.0
ARP244	154.83/94	3.2	- *	1.85 ^{+0.2} _{-0.2}	10.4 ^{+3.0} _{-2.6}	0.62 ^{+0.02} _{-0.03}	0.490 ^{+0.490} _{-0.075}	33/40.4
NGC4051	118.05/99 ^(H)	1.2	18.5 ^{+2.7} _{-2.6}	2.14 ^{+0.1} _{-0.2}	337 ⁺¹¹⁹ ₋₁₁₂	-	-	531/40.9
NGC4151	131.63/90 ^(H)	2.1	5.96 ^{+0.29} _{-0.46}	1.57 ^{+0.05} _{-0.06}	1030 ⁺¹¹² ₋₁₀₃	-	-	4678/42.1
NGC4214	69.47/49	1.9	0.0640 ^{+0.02} _{-0.02}	1.9 [†]	4.36 ^{+0.93} _{-0.93}	0.30 ^{+0.07} _{-0.04}	0.566 ^{+0.610} _{-0.192}	13/38.9
NGC4253	2280.28/143 ^(D)	1.8	- *	2.08 ^{+0.02} _{-0.02}	1030 ⁺²³ ₋₂₃	0.21	0.19	2461/43.0
MESSIER099	66.3/37	2.9	-	1.9 [†]	2.19 ^{+0.71} _{-0.71}	0.32 ^{+0.02} _{-0.02}	2.36 ^{+2.37} _{-0.17}	7/40.0
MESSIER100	114/70	2	-	1.9 [†]	6.01 ^{+0.79} _{-0.79}	0.63 ^{+0.03} _{-0.03}	2.85 ^{+2.90} _{-0.55}	19/40.1
NGC4388	163.61/127	2.6	39.7 ^{+6.6} _{-13.1}	1.60 ^{+0.1} _{-0.2}	1040 ⁺⁴⁵⁰ ₋₃₀₂	0.77 ^{+0.09} _{-0.11}	0.0033 ^{+0.009} _{-0.001}	2109/42.9
NGC4414	89.07/55	1.6	- *	1.9 [†]	5.71 ^{+0.71} _{-0.71}	0.46 ^{+0.05} _{-0.07}	0.562 ^{+0.563} _{-0.073}	17/39.3
NGC4449	62/67	1.4	0.0166 ^{+0.0180} _{-0.0128}	1.9 [†]	9.83 ^{+9.26} _{-9.26}	-	-	29/38.5

Name (1)	χ^2/DOF (2)	N_{Gal} (3)	$N_{\text{H},1}$ (4)	Γ_1 (5)	norm (6)	kT_{therm} (7)	R_{therm} (8)	$F_{\text{HX}}/L_{\text{HX}}$ (9)
3C273	1161.87/145 ^(D)	1.8	-	1.58 ^{+0.01} _{-0.01}	1950 ⁺²¹ ₋₂₀	0.99	0.04	9724/45.8
NGC4490	50.39/60	1.8	0.204 ^{+0.023} _{-0.053} *	2.06 ^{+0.3} _{-0.3}	16.5 ^{+8.6} _{-5.7}	0.60 ^{+0.24} _{-0.23}	0.112 ^{+0.134} _{-0.082}	38/39.5
MESSIER088	6.77/9 ^(F)	2.6	0.185 ^{+0.274} _{-0.053}	4.05 ⁺² ₋₁	7.28 ^{+9.27} _{-3.57}	0.77 ^{+0.26} _{-0.52}	0.190 ^{+0.318} _{-0.171}	12/41.7
NGC4559	117.77/100	1.5	0.110 ^{+0.02} _{-0.01} *	2.13 ^{+0.2} _{-0.1}	23.9 ^{+5.1} _{-3.3}	-	-	50/39.9
MESSIER090	134.05/77	2.8	-	1.9 [†]	3.36 ^{+0.40} _{-0.40}	0.63 ^{+0.02} _{-0.02}	0.966 ^{+0.967} _{-0.046}	10/37.3
MESSIER058	185.3/134	2.8	-	1.78 ^{+0.1} _{-0.09}	98.2 ^{+13.6} _{-11.6}	0.71 ^{+0.03} _{-0.05}	0.911 ^{+0.918} _{-0.109}	391/41.4
NGC4593	168.95/142	1.9	<0.0156*	1.83 ^{+0.05} _{-0.05}	1060 ⁺⁷³ ₋₆₈	0.21 ^{+0.01} _{-0.01}	0.0498 ^{+0.0918} _{-0.0502}	3795/42.8
MESSIER104	176.27/110	3.6	0.0673 ^{+0.022} _{-0.018} *	1.95 ^{+0.1} _{-0.1}	50.6 ^{+9.2} _{-8.5}	-	-	139/38.9
NGC4631	60.79/54	1.3	0.214 ^{+0.043} _{-0.079} *	1.9 [†]	2.95 ^{+0.39} _{-0.36}	0.34 ^{+0.08} _{-0.04}	1.16 ^{+1.44} _{-0.50}	9/38.9
NGC4666	167.4/100	1.7	-	1.9 [†]	8.60 ^{+0.80} _{-0.71}	0.47 ^{+0.06} _{-0.06}	0.292 ^{+0.012} _{-0.025}	30/40.5
NGC4725	32.38/26	0.9	-	1.9 [†]	1.65 ^{+0.73} _{-0.73}	0.59 ^{+0.06} _{-0.06}	0.399 ^{+0.126} _{-0.1668}	5/39.2
UGC08058	123.59/73 ^(F)	1	7.07 ^{+1.82} _{-1.36}	1.66 ^{+0.1} _{-0.08}	16.3 ^{+6.9} _{-2.4}	0.79 ^{+0.02} _{-0.07}	0.0901 ^{+0.068} _{-0.0307}	60/42.5
NGC4968	22.37/14	8.4	300 ⁻¹²³	1.9 [†]	2540 ⁺¹⁰⁰⁰⁰ ₋₂₀₄₀	-	-	26/43.2
NGC5005	88.07/51	1.1	-	1.57 ^{+0.3} _{-0.3}	7.14 ^{+4.32} _{-2.84}	0.72 ^{+0.03} _{-0.08}	0.997 ^{+0.999} _{-0.072}	36/39.9
MESSIER063	59.41/40	1.3	0.0405 ^{+0.026} _{-0.015} *	1.9 [†]	7.55 ^{+1.38} _{-1.38}	0.30 ^{+0.02} _{-0.02}	1.14 ^{+1.15} _{-0.19}	21/39.2
MCG-03-34-064	271.88/139	5.2	40.0 ^{+5.2} _{-1.8}	2.50 ^{+0.3} _{-0.2}	1160 ⁺¹⁰⁹⁰ ₋₃₇₅	0.80 ^{+0.02} _{-0.02}	0.007 ^{+0.007} _{-0.000}	258/42.9
NGC5170	30.92/28	7	0.145 ^{+0.063} _{-0.046}	1.9 [†]	1.21 ^{+0.55} _{-0.55}	-	-	4/39.3
NGC5194	101.54/67	1.8	0.0377 ^{+0.007} _{-0.006} *	2.61 ^{+0.2} _{-0.3}	20.2 ^{+15.1} _{-9.7}	0.64 ^{+0.01} _{-0.01}	0.964 ^{+0.721} _{-0.282}	42/40.4
ESO383-G035	176.91/96 ^(H)	3.9	-	2.09 ^{+0.03} _{-0.03}	1910 ⁺⁸⁷ ₋₈₁	-	-	4033/42.8
MESSIER083	162.35/88	4	-	2.00 ^{+0.2} _{-0.2}	15.5 ^{+4.3} _{-4.3}	0.71 ^{+0.01} _{-0.01}	1.44 ^{+1.44} _{-0.06}	40/39.4
IRAS13349+2438	227.52/125	1	1.04 ^{+0.24} _{-0.19} *	2.31 ^{+0.07} _{-0.06}	229 ⁺¹⁰⁷ ₋₇₁	0.22 ^{+0.00} _{-0.01}	1.03 ^{+0.20} _{-0.19}	217/43.8
NGC5256	82.96/49 ^(F)	1.5	17.5 ^{+5.6} _{-3.8}	2.74 ^{+0.3} _{-0.2}	99.8 ^{+55.3} _{-31.2}	0.80 ^{+0.03} _{-0.04}	0.0413 ^{+0.0238} _{-0.0145}	30/42.2
NGC5253	8.3/6 ^(H)	4	-	1.9 [†]	0.490 ^{+0.283} _{-0.283}	-	-	2/37.9
MRK0273	54.16/54	0.9	59.7 ^{+17.1} _{-12.8}	1.9 [†]	70.1 ^{+31.9} _{-19.0}	0.72 ^{+0.06} _{-0.07}	0.0277 ^{+0.0129} _{-0.0046}	37/42.8
IC4329A	112.97/97 ^(H)	4.6	-	1.67 ^{+0.01} _{-0.01}	2160 ⁺²⁸ ₋₂₇	-	-	9544/43.7
UGC08850	101.22/79	2	38.7 ^{+9.2} _{-5.7}	1.9 [†]	78.2 ^{+20.9} _{-6.4}	0.71 ^{+0.04} _{-0.09}	0.0323 ^{+0.0235} _{-0.0039}	63/43.1
NGC5506	273.02/149	4	3.24 ^{+0.24} _{-0.24}	1.82 ^{+0.05} _{-0.04}	2440 ⁺²⁰⁵ ₋₁₈₇	-	-	6816/42.8
NGC5548	675.17/142 ^(D)	1.6	0.01*	1.64 ^{+0.01} _{-0.02}	874 ⁺²⁰ ₋₂₅	0.2	0.14	4061/43.4
NGC5775	45.72/43	3.6	0.525 ^{+0.300} _{-0.455} *	1.9 [†]	2.38 ^{+0.53} _{-0.53}	0.29 ^{+0.03} _{-0.04}	5.64 ^{+8.80} _{-3.19}	6/39.8
2MASXJ15115979	252.79/145	8.3	0.0657 ^{+0.0035} _{-0.0034}	1.67 ^{+0.09} _{-0.07}	198 ⁻¹⁹	-	-	858/43.9
VV705	26.5/18 ^(F)	1.9	85.9 ^{-62.2}	1.9 [†]	19.8 ⁺¹⁶⁸⁰ _{-17.3}	0.32 ^{+0.26} _{-0.07}	0.0248 ^{+2.11} _{-0.0280}	12/42.3
UGC09944	33.35/31	2.8	0.362 ^{+0.543} _{-0.277}	5.66 ⁺⁴ ₋₂	11.7 ^{+32.5} _{-6.7}	0.81 ^{+0.07} _{-0.06}	1.85 ^{+0.53} _{-0.34}	5/41.6
2MASXJ15504152	5.54/4 ^(F)	9	112 ⁺²⁰ ₋₁₀	1.9 [†]	747 ⁺²⁸⁴ ₋₁₅₁	0.79 ^{+0.04} _{-0.04}	0.0839 ^{+0.099} _{-0.0500}	45/43.0
NGC6240	177.15/111	5	< 0.04	1.9 [†]	1.57 ^{+0.94} _{-0.71}	0.70 ^{+0.10} _{-0.13}	1.72 ^{+1.27} _{-0.92}	191/43.5
NGC6286	8.34/5 ^(F)	1.8	-	1.9 [†]	1.41 ^{+0.51} _{-0.54}	0.23 ^{+0.04} _{-0.04}	1.53 ^{+0.78} _{-0.73}	5/40.6
NGC6552	19.13/18 ^(F)	3.9	-	1.9 [†]	22.6 ^{+25.8} _{-16.3}	0.58 ^{+0.20} _{-0.20}	0.0563 ^{+0.180} _{-0.0295}	49/42.9
AM1925-724	43.51/54	5.2	38.1 ^{+39.2} _{-21.7}	1.9 [†]	2.58 ^{+16.3} _{-4.69}	0.61 ^{+0.23} _{-0.22}	4.33 ^{+4.04} _{-1.00}	25/42.8
NGC6810	85.94/61	5	-	1.9 [†]	6.58 ^{+1.66} _{-2.03}	-	-	8/39.9
NGC6890	2.06/4 ^(F)	2.9	0.106 ^{+0.201} _{-0.086}	3.87 ⁺² ₋₁	901 ⁺²¹ ₋₂₂	0.03	248	28/42.2
MRK0509	550.93/138 ^(D)	4.2	-	1.73 ^{+0.02} _{-0.02}	15.7 ⁺¹⁰⁰⁰⁰ _{-10.9}	0.61 ^{+0.12} _{-0.34}	0.103 ^{+0.53} _{-0.026}	3660/44.0
ESO286-IG019	41.66/33	3.3	48.7 ^{+25.8} _{-35.2}	1.9 [†]	1.11 ^{+6.36} _{-1.11}	-	-	11/42.3
NGC7090	125.36/134 ^(F)	2.4	0.136 ^{+53.9} _{-0.136}	1.9 [†]	-	-	-	38/39.8

Name (1)	χ^2/DOF (2)	N_{Gal} (3)	$N_{\text{H},1}$ (4)	Γ_1 (5)	norm (6)	kT_{therm} (7)	R_{therm} (8)	$F_{\text{HX}}/L_{\text{HX}}$ (9)
NGC7172	254.94/153	1.9	8.50 ^{+0.27} _{-0.39}	1.54 ^{+0.06} _{-0.07}	611 ⁺⁴³ ₋₅₂	-	-	2108/42.7
NGC7213	186.15/146	1.1	-	1.69 ^{+0.02} _{-0.02}	520 ⁺¹⁷ ₋₁₇	0.068 ^{+0.003} _{-0.009}	0.743 ^{+0.776} _{-0.131}	2194/42.7
IC5169	6.01/5	1.1	- *	1.9 [†]	7.30 ^{+5.39} _{-5.39}	-	-	21/40.7
NGC7252	50.76/34	2	-	1.9 [†]	1.24 ^{+0.45} _{-0.45}	0.47 ^{+0.06} _{-0.07}	1.38 ^{+1.39} _{-0.16}	4/40.4
3C445	157.17/139 ^(F)	4.5	35.0 ^{+10.8} _{-7.7}	1.59 ^{+0.2} _{-0.2}	238 ⁺⁷² ₋₇₂	0.14 ^{+0.03} _{-0.02}	0.0170 ^{+0.020} _{-0.0066}	687/43.9
NGC7314	233.2/140	0.1	0.600 ^{+0.013} _{-0.027} *	1.95 ^{+0.02} _{-0.01}	1500 ⁺²⁴ ₋₁₄	0.22 ^{+0.02} _{-0.02}	0.00961 ^{+0.008} _{-0.001}	4008/42.3
MCG-03-58-007	14.01/20	2	27.5 ^{+7.9} _{-6.2}	1.9 [†]	89.2 ^{+26.8} _{-20.5}	0.29 ^{+0.10} _{-0.09}	0.0313 ^{+0.0347} _{-0.0142}	91/42.7
NGC7469	417.02/143 ^(D)	4.4	0.04*	1.86 ^{+0.02} _{-0.02}	862 ⁺²⁰ ₋₁₉	0.22	0.121 ^{+0.171} _{-0.00}	2955/43.2
NGC7479	15.82/17	5.4	201 ⁺⁴⁹³ ₋₁₂₂	1.9 [†]	263 ⁺³³³⁰ ₋₂₈₅	0.39 ^{+0.16} _{-0.13}	0.0104 ^{+0.022} _{-0.0046}	33/42.0
ESO148-IG002	17.55/24	1.6	- *	1.9 [†]	2.72 ^{+1.08} _{-0.59}	0.65 ^{+0.11} _{-0.10}	0.399 ^{+0.188} _{-0.175}	17/43.2
NGC7552	31.36/19 ^(F)	1.3	-	1.9 [†]	8.09 ^{+1.41} _{-1.39}	0.76 ^{+0.06} _{-0.10}	1.16 ^{+0.60} _{-0.53}	25/40.2
NGC7582	353.48/130 ^(F)	1.3	0.04	2.35	11	-	-	223/42.6
NGC7674	64.74/36 ^(F)	4.2	-	3.28 ⁺² _{-0.3}	5.11 ^{+1.78} _{-1.63}	0.79 ^{+0.08} _{-0.12}	0.0918 ^{+10.3} _{-0.0983}	60/43.6
NGC7714	82.16/51	5	0.137 ^{+0.048} _{-0.031}	1.9 [†]	5.34 ^{+0.81} _{-0.81}	0.59 ^{+0.06} _{-0.06}	11.9 ^{+16.0} _{-4.3}	17/40.5
NGC7771	53/59	4	0.05 ^{+0.06} _{-0.05} *	1.68 ^{+0.3} _{-0.3}	4.26 ^{+0.50} _{-1.48}	0.59 ^{+0.04} _{-0.04}	0.525 ^{+0.530} _{-0.064}	18/40.9
MIRK0331	32.32/30	4	0.123 ^{+0.120} _{-0.055}	1.9 [†]	1.79 ^{+0.64} _{-0.64}	0.73 ^{+0.05} _{-0.05}	1.45 ^{+1.46} _{-0.19}	6/40.7

Table 4. Parameters of the second power-law component, if it is present. Column (1) Galaxy name; Column (2) the neutral column density measured in the secondary power-law (10^{22} cm^{-2}); Column (3) the power-law index of the secondary power-law; Column (4) the ratio of the normalisation of the second power-law to the primary power-law.

Name (1)	$N_{\text{H},2}$ (2)	Γ_2 (3)	F_{pl} (4)
NGC0017	0.0212 $^{+0.0180}_{-0.0145}$	= Γ_1	0.0740 $^{+0.0112}_{-0.0112}$
NGC0214	-	= Γ_1	0.0623 $^{+0.0363}_{-0.0248}$
NGC0262	-	1.80 $^{+0.2}_{-0.1}$	0.00530 $^{+0.0039}_{-0.0041}$
NGC0424	0.0334 $^{+0.0220}_{-0.0179}$	3.05 $^{+0.3}_{-0.3}$	0.292 $^{+0.046}_{-0.041}$
NGC0526A	0.0946 $^{+0.0174}_{-0.0171}$	2.04 $^{+0.2}_{-0.2}$	0.0303 $^{+0.0045}_{-0.0042}$
NGC0513	0.0816 $^{+0.0926}_{-0.0596}$	2.16 $^{+0.7}_{-0.5}$	0.0331 $^{+0.0154}_{-0.0095}$
NGC1052	6.29 $^{+1.30}_{-1.94}$	= Γ_1	0.766 $^{+0.361}_{-0.351}$
ARP118	0.176 $^{+0.182}_{-0.116}$	4.11 $^{+1}_{-0.9}$	0.00842 $^{+0.00857}_{-0.00370}$
MCG-02-08-039	-	= Γ_1	0.0196 $^{+0.0033}_{-0.0033}$
NGC1194	-	= Γ_1	0.0220 $^{+0.0112}_{-0.0110}$
NGC1320	0.0341 $^{+0.0155}_{-0.0133}$	3.36 $^{+0.2}_{-0.2}$	0.0110 $^{+0.0012}_{-0.0011}$
NGC1365	-	= Γ_1	0.03
NGC1482	0.101 $^{+0.066}_{-0.057}$	= Γ_1	0.412 $^{+0.804}_{-0.308}$
NGC1667	-	= Γ_1	0.00585 $^{+0.981}_{-0.00583}$
NGC1808	0.164 $^{+0.013}_{-0.013}$	= Γ_1	0.868 $^{+0.120}_{-0.046}$
ESO362-G018	-	1.78 $^{+0.07}_{-0.06}$	0.433 $^{+0.020}_{-0.015}$
2MASXJ05210136	0.0187 $^{+0.0171}_{-0.0151}$	3.42 $^{+0.3}_{-0.3}$	0.02 $^{+0.07}_{-0.12}$
IC0450	-	2.59 $^{+0.3}_{-1}$	0.292 $^{+0.025}_{-0.116}$
NGC2655	0.0325 $^{+0.0777}_{-0.0325}$	2.60 $^{+0.8}_{-0.6}$	0.0422 $^{+0.0234}_{-0.0136}$
MRK0704	-	3.04 $^{+0.1}_{-0.1}$	0.190 $^{+0.067}_{-0.043}$
UGC05101	0.199 $^{+0.111}_{-0.062}$	= Γ_1	0.0498 $^{+0.0498}_{-0.00}$
NGC3227	-	= Γ_1	0.123 $^{+0.006}_{-0.005}$
NGC3516	2.98 $^{+0.42}_{-0.39}$	= Γ_1	0.669 $^{+0.204}_{-0.144}$
NGC3982	0.06	2.87	0.24
NGC4013	0.0350 $^{+0.0444}_{-0.0254}$	= Γ_1	0.238 $^{+0.045}_{-0.047}$
NGC4051	-	= Γ_1	0.498 $^{+0.177}_{-0.166}$
NGC4388	18.7 $^{+2.1}_{-9.4}$	= Γ_1	0.409 $^{+0.240}_{-0.230}$
UGC08058	-	= Γ_1	0.184 $^{+0.079}_{-0.027}$
NGC4968	-	= Γ_1	0.00101 $^{+0.00016}_{-0.00016}$
MCG-03-34-064	0.0161 $^{+0.0090}_{-0.0081}$	2.73 $^{+0.09}_{-0.08}$	0.0147 $^{+0.0008}_{-0.0008}$
IRASF13349+2438	-	4.17 $^{+0.1}_{-0.1}$	0.743 $^{+0.0791}_{-0.0644}$
NGC5256	0.0269 $^{+0.0171}_{-0.0128}$	= Γ_1	0.0535 $^{+0.0296}_{-0.0167}$
MRK0273	-	= Γ_1	0.0341 $^{+0.0037}_{-0.0037}$
UGC08850	-	= Γ_1	0.0364 $^{+0.0031}_{-0.0031}$
NGC5506	0.0910 $^{+0.0124}_{-0.0116}$	= Γ_1	0.0183 $^{+0.0012}_{-0.0011}$
VV705	0.212 $^{+0.229}_{-0.107}$	= Γ_1	0.121 $^{+10.3}_{-0.106}$
NGC6240	0.168 $^{+0.019}_{-0.018}$	= Γ_1	0.0376 $^{+0.0026}_{-0.0026}$
AM1925-724	0.172 $^{+0.071}_{-0.058}$	= Γ_1	0.144 $^{+0.023}_{-0.022}$
ESO286-IG019	0.0347 $^{+0.0554}_{-0.0347}$	= Γ_1	0.0666 $^{+0.0268}_{-0.0255}$
NGC7172	0.133 $^{+0.035}_{-0.031}$	3.00 $^{+0.3}_{-0.3}$	0.00593 $^{+0.00079}_{-0.00067}$
3C445	0.00489 $^{+0.0218}_{-0.00489}$	= Γ_1	0.0352 $^{+0.0255}_{-0.0116}$
NGC7314	0.150 $^{+0.012}_{-0.038}$	4.15 $^{+0.3}_{-0.8}$	0.00672 $^{+0.00262}_{-0.00059}$
MCG-03-58-007	-	3.37 $^{+0.4}_{-0.4}$	0.0251 $^{+1000}_{-0.0097}$
NGC7479	0.0888 $^{+0.201}_{-0.0888}$	3.05 $^{+2}_{-1}$	0.00643 $^{+0.00925}_{-0.00337}$

Table 5. Parameters of the soft excess component, if it is present. Column (1) Galaxy name; Column (2) the ratio of the data at 0.4 keV to the extrapolated 2.5-10 keV power-law. * 3C120 has a soft excess which does not fit our criteria, as it does not have a data/model ratio greater than 20% at 0.4 keV. However, this source has a clear soft excess at 0.7 keV not well modelled by thermal plasma emission. We find that a ratio of 3.2 at 0.4 keV is recovered when an additional intrinsic absorption component is used; Column (3) the model used; Column (4) the input soft photon (Wien) temperature (compTT model only, keV); Column (5) the temperature (keV); Column (6) the plasma optical depth (compTT model only); Column (7) the ratio of the normalisation of this component to the normalisation of the primary power-law.

Name (1)	d/m (0.4 keV) (2)	model (3)	T ₀ (4)	kT (5)	τ _p (6)	F _{SX} (7)
MRK0335	2.67	compTT	0.05	90.7	0.01	0.22
MRK0618	1.59	compTT	0.0941 ^{+0.0117} _{-0.0142}	2.00 ^{+4.47} _{-0.00}	2.73 ^{+0.24} _{-1.63}	2.29 ^{+2.45} _{-1.89}
3C120	3.20*	compTT	0.09	69.0	0.01	0.11
UGC03973	2.37	compTT	0.0510 ^{+0.0548} _{-0.0281}	2.01 ^{+3.05} _{-0.01}	3.38 ^{+0.14} _{-1.25}	14.8 ^{+22.2} _{-12.6}
IRASF07599+6508	2.46	body	-	0.13 ^{+0.02} _{-0.02}	-	0.0524 ^{+0.0532} _{-0.0116}
MESSIER081	1.29	compTT	0.137 ^{+0.009} _{-0.009}	2.00 ^{+9.70} _{-0.00}	2.75 ^{+0.16} _{-2.39}	0.487 ^{+0.489} _{-0.473}
NGC4253	1.62	compTT	0.08	34.1	0.1	0.17
3C273	2.1	compTT	0.06	66.2	0.03	0.14
NGC4593	1.64	compTT	0.00743 ^{+0.0257} _{-0.00486}	2.06 ^{+0.85} _{-0.06}	3.17 ^{+0.27} _{-0.55}	590 ⁺⁶¹⁵ ₋₅₅₈
NGC4725	3.83	body	-	0.11 ^{+0.02} _{-0.02}	-	0.0676 ^{+0.0679} _{-0.0087}
NGC5548	1.61	compTT	0.02	26.5	0.27	4.44
UGC09944	7.8	body	-	0.10 ^{+0.01} _{-0.01}	-	0.136 ^{+0.138} _{-0.014}
MRK0509	2.87	compTT	0.07	44.6	0.11	0.25
NGC7213	1.3	compTT	0.146 ^{+0.011} _{-0.009}	44.9 ^{+12.1} _{-42.9}	0.0100 ^{+0.582} _{-0.00}	0.0141 ^{+0.124} _{-0.0025}
NGC7469	2.15	compTT	0.02	40.8	0.07	8.78

Table 6. Parameters of the reflection component, if it is present. Column (1) Galaxy name; Column (2) power-law index of the reflection component; Column (3) the ratio of the normalisation of the *pexmon* component to the normalisation of the primary power-law; Column (4) the ratio of the normalisation of the *torus* component to the normalisation of the primary power-law. Presented only where $R_{pexmon} > 1$; Column (5) The intrinsic 2-10 keV luminosity as determined from the *pexmon* component; Column (6) The intrinsic 2-10 keV luminosity as determined from the *torus* component.

Name (1)	Γ_2 (2)	R_{pexmon} (3)	R_{torus} (4)	L_{HX} (<i>pexmon</i>) (5)	L_{HX} (<i>torus</i>) (6)
MRK0335	2.03	0.308 ^{+0.115} _{-0.116}	-	-	-
NGC0424	= Γ_1	9.72 ^{+218.} _{-9.02}	24.9	42.5	43.1
NGC0526A	= Γ_1	0.193 ^{+0.105} _{-0.100}	-	-	-
NGC0513	= Γ_1	0.955 ^{+1.09} _{-1.01}	-	-	-
NGC1068	= Γ_1	10.3	31.0	42.2	42.4
ARP118	= Γ_1	0.501 ^{+0.189} _{-0.213}	-	-	-
NGC1194	= Γ_1	49.8 ^{+45.8} _{-45.9}	167.0	42.3	43.0
NGC1320	= Γ_1	40.4 ^{+44.9} _{-39.0}	109.0	42.7	42.3
NGC1386	1.9 [†]	145 ⁺¹⁶⁰ ₋₁₄₇	615.0	40.9	41.7
3C120	= Γ_1	0.156 ^{+0.116} _{-0.143}	-	-	-
MRK0618	= Γ_1	0.379 ^{+0.507} _{-0.381}	-	-	-
ESO362-G018	= Γ_1	5.47 ^{+5.24} _{-6.11}	11.4	42.4	42.4
IC0450	= Γ_1	0.441 ^{+0.209} _{-0.168}	-	-	-
MRK0704	= Γ_1	0.285 ^{+0.708} _{-0.290}	-	-	-
NGC2992	= Γ_1	0.220 ^{+0.089} _{-0.109}	-	-	-
MESSIER081	= Γ_1	0.302 ^{+0.105} _{-0.120}	-	-	-
NGC3079	1.9 [†]	16.3 ^{+7.8} _{-9.7}	30.9	40.9	41.2
NGC3147	= Γ_1	0.139 ^{+1.22} _{-0.141}	-	-	-
NGC3227	= Γ_1	5.21 ^{+3.02} _{-3.54}	12.4	41.6	42.0
NGC4051	= Γ_1	1.53 ^{+1.04} _{-1.55}	9.0	40.9	41.5
NGC4151	= Γ_1	0.785 ^{+0.110} _{-0.306}	-	-	-
NGC4253	2.08	0.413 ^{+0.082} _{-0.077}	-	-	-
MESSIER088	1.9 [†]	17.6 ^{+24.2} _{-17.6}	17.5	41.7	41.7
MESSIER058	= Γ_1	0.872 ^{+0.703} _{-0.571}	-	-	-
NGC4593	= Γ_1	0.888 ^{+0.299} _{-0.256}	-	-	-
NGC4631	= Γ_1	1.16 ^{+2.01} _{-1.16}	0.8	38.9	38.8
NGC4666	= Γ_1	2.02 ^{+1.58} _{-1.71}	8.9	40.5	41.1
NGC5194	= Γ_1	51.3 ^{+31.6} _{-41.1}	177.0	40.4	40.9
ESO383-G035	= Γ_1	0.212 ^{+0.066} _{-0.068}	-	-	-
IC4329A	= Γ_1	0.274 ^{+0.056} _{-0.069}	-	-	-
NGC5506	= Γ_1	0.270 ^{+0.147} _{-0.153}	-	-	-
NGC5548	1.64	0.162 ^{+0.134} _{-0.162}	-	-	-
2MASXJ15504152	1.9 [†]	13.7 ^{+59.5} _{-8.9}	56.7	43.0	43.6
NGC6552	= Γ_1	112 ⁺⁸³ ₋₄₈	1020.0	42.9	43.6
NGC6890	1.9 [†]	52.1 ^{+43.2} _{-47.0}	76.6	42.2	42.3
MRK0509	= Γ_1	0.309 ^{+0.062} _{-0.071}	-	-	-
NGC7172	= Γ_1	0.255 ^{+0.102} _{-0.256}	-	-	-
3C445	= Γ_1	0.317 ^{+2.74} _{-0.152}	-	-	-
NGC7314	= Γ_1	0.131 ^{+0.115} _{-0.117}	-	-	-
NGC7469	= Γ_1	0.698 ^{+0.087} _{-0.083}	-	-	-
NGC7479	= Γ_1	0.293 ^{+3.71} _{-0.295}	-	-	-
ESO148-IG002	= Γ_1	41.6 ^{+32.6} _{-43.1}	45.3	43.2	43.2
NGC7582	1.49	107	400.0	42.6	42.5
NGC7674	1.91 ^{+0.31} _{-0.37}	143 ⁺¹²⁰ ₋₁₄₈	185.0	43.6	43.7

Table 7. X-ray spectral fitting data. Parameters of the warm absorber, if it is present. Column (1) Galaxy name; Column (2) the logarithm of the ionised column density (cm^{-2}); Column (3) the logarithm of the ionisation parameter, ξ .

Name (1)	$\log_{10} N_{\text{H}}$ (2)	$\log_{10} \xi$ (3)
MRK0335	22.9	3.88
NGC0262	22.3 ^{+0.8} _{-0.2}	3.26 ^{+0.74} _{-0.25}
NGC0526A	21.4 ^{+0.4} _{-0.6}	2.49 ^{+0.19} _{-0.21}
NGC0520	21.9 ^{+0.3} _{-0.2}	-4.00 ^{+1.28} _{-0.00}
2MASXJ01500266	21.4 ^{+0.3} _{-0.1}	-0.680 ^{0.40} _{-0.55}
NGC0695	21.9 ^{+0.3} _{-0.4}	0.246 ^{+0.738} _{-0.00}
NGC1052	23.0 ^{+0.2} _{-0.1}	2.71 ^{+0.21} _{-0.23}
NGC1194	22.2 ^{+0.2} _{-0.4}	0.884 ^{+0.226} _{-0.00}
NGC1291	21.2 ^{+0.0} _{-0.1}	-3.90 ^{0.25} _{-0.10}
MRK0618	20.7 ^{+0.5} _{-0.6}	-0.161 ^{0.662} _{-0.26}
ESO362-G018	22.3 ^{+0.3} _{-0.7}	3.00 ^{+0.32} _{-0.19}
IC0450	21.9 ^{+0.0} _{-0.3}	0.119 ^{+0.082} _{-0.028}
UGC03973	21.1 ^{+0.0} _{-0.1}	-3.64 ^{+0.04} _{-0.36}
MRK0704	23.0 ^{+0.1} _{-0.1}	2.44 ^{+0.15} _{-0.16}
NGC3227	21.4 ^{+0.1} _{-0.0}	-1.09 ^{+0.05} _{-0.03}
MESSIER066	21.7 ^{+1.5} _{-1.7}	1.66 ^{+2.34} _{-0.00}
NGC3976	21.6 ^{+0.4} _{-0.4}	-3.82 ^{+0.66} _{-0.18}
NGC4013	22.8 ^{+1.1} _{-0.3}	-1.37 ^{+5.08} _{-2.63}
ARP244	20.9 ^{+0.1} _{-0.1}	-3.20 ^{+0.08} _{-0.33}
NGC4253	20.9	-4
NGC4414	21.1 ^{+0.2} _{-0.2}	-2.90 ^{+0.08} _{-0.01}
NGC4490	20.7 ^{+0.4} _{-0.7}	-2.40 ^{+6.40} _{-1.60}
NGC4559	20.7 ^{+0.1} _{-0.2}	-3.64 ^{+2.44} _{-0.36}
NGC4593	21.3 ^{+0.1} _{-0.2}	1.82 ^{+0.07} _{-0.05}
MESSIER104	20.9 ^{+0.1} _{-0.4}	-0.285 ^{+0.164} _{-0.329}
NGC4631	21.1 ^{+0.3} _{-1.1}	0.836 ^{+3.16} _{-0.00}
NGC4666	21.8 ^{+0.0} _{-0.0}	0.564 ^{+0.043} _{-0.082}
MESSIER063	23.4 ^{+0.1} _{-1.2}	3.84 ^{+0.16} _{-1.01}
NGC5194	23.5 ^{+0.0} _{-0.1}	2.83 ^{+0.27} _{-0.20}
MESSIER083	22.1 ^{+0.2} _{-0.3}	2.40 ^{+0.11} _{-0.16}
IRASF13349+2438	21.1 ^{+0.1} _{-0.1}	-1.62 ^{+0.05} _{-0.1}
NGC5548	20.8	-4
NGC5775	21.6 ^{+0.1} _{-0.5}	-3.14 ^{+0.33} _{-0.08}
MRK0509	20.2	2.06
IC5169	21.3 ^{+0.5} _{-0.0}	-3.94 ^{+0.55} _{-0.06}
NGC7314	20.9 ^{+0.1} _{-0.2}	2.08 ^{+0.20} _{-0.08}
NGC7469	20.8	2.2
ESO148-IG002	21.3 ^{+0.4} _{-0.1}	-3.93 ^{+3.87} _{-0.07}
NGC7771	21.1 ^{+0.2} _{-0.1}	-3.67 ^{+0.33} _{-0.33}

Table 8. Parameters of the iron $K\alpha$ line, be it narrow or broad, if it is present. Column (1) Galaxy name; Column (2) the EW of the narrow line at 6.4 keV modelled by either **trans** or **pevxmon**; Column (3) the energy of the line constrained to be between 6.2 and 6.6 keV, not associated with any other component; Column (4) the gaussian width of this component; Column (5) the EW of this component.

Name (1)	EW _{6.4} (2)	E _{FeKα} (3)	σ _{FeKα} (4)	EW _{FeKα} (5)
MRK0335	31 ⁺⁸ ₋₈	6.51 ^{+0.09} _{-0.11}	0.42 ^{+0.44} _{-0.13}	134 ⁺⁴² ₋₃₈
NGC0017	214 ⁺²⁴⁰ ₋₂₁₄	-	-	-
NGC0262	28 ⁺⁷ ₋₇	-	-	-
UGC00545	-	6.6 ^{+0.0} _{-0.1}	0.31 ^{+0.33} _{-0.2}	143 ⁺⁹⁰ ₋₇₃
NGC0424	576 ⁺¹⁸⁷ ₋₁₈₇	6.51 ^{+0.09} _{-0.31}	< 1	109 ⁺²²⁴ ₋₁₀₉
NGC0526A	26 ⁺⁹ ₋₉	6.5 ^{+0.1} _{-0.1}	0.34 ^{+0.39} _{-0.1}	99 ⁺³⁸ ₋₃₆
NGC0513	116 ⁺⁴⁸ ₋₄₈	6.2 ^{+0.2} _{-0.0}	< 0.35	48 ⁺¹⁶⁶ ₋₃₉
2MASXJ01500266	-	6.72 ^{+0.26} _{-0.23}	0.28 ^{+0.43} _{-0.28}	715 ⁺⁶²⁸ ₋₄₄₈
NGC1052	124 ⁺²³ ₋₂₃	6.51 ^{+0.09} _{-0.11}	0.05 ^{+0.26} _{-0.05}	23 ⁺⁹⁵ ₋₁₁
NGC1068	281	6.6	0.18	396
ARP118	60 ⁺²¹ ₋₂₁	6.47 ^{+0.13} _{-0.08}	0.04 ^{+0.16} _{-0.04}	40 ⁺⁴³ ₋₃₄
MCG-02-08-039	220 ⁺¹⁴⁰ ₋₁₄₀	-	-	-
NGC1194	194 ⁺⁴⁶ ₋₄₆	6.6 ^{+0.0} _{-0.1}	0.26 ^{+0.36} _{-0.13}	239 ⁺¹⁷⁹ ₋₁₇₄
NGC1313	28 ⁺⁶² ₋₂₈	-	-	-
NGC1320	701 ⁺¹⁶³ ₋₁₆₃	6.5 ^{+0.1} _{-0.1}	0.06 ^{+0.09} _{-0.06}	239 ⁺²⁰⁹ ₋₁₃₈
NGC1365	78	-	-	-
NGC1386	1710 ⁺³⁷³ ₋₃₇₃	-	-	-
3C120	19 ⁺⁵ ₋₅	6.43 ^{+0.08} _{-0.04}	0.15 ^{+0.22} _{-0.05}	47 ⁺²¹ ₋₁₆
MRK0618	30 ⁺³⁷ ₋₃₀	6.2 ^{+0.2} _{-0.0}	< 1.77	45 ⁺⁴⁰⁴ ₋₄₁
NGC1808	10 ⁺⁵² ₋₁₀	-	-	-
ESO362-G018	257 ⁺⁶³ ₋₆₃	6.54 ^{+0.06} _{-0.08}	0.12 ^{+0.51} _{-0.12}	108 ⁺¹⁸⁹ ₋₈₆
2MASXJ05210136	71 ⁺⁵⁶ ₋₅₆	-	-	134 ⁺⁷² ₋₇₂
2MASXJ05580206	-	6.37 ^{+0.16} _{-0.17}	0.11 ^{+0.48} _{-0.11}	45 ⁺³⁰ ₋₄₀
IC0450	63 ⁺²⁰ ₋₂₀	-	-	-
UGC03973	-	6.43 ^{+0.07} _{-0.06}	0.11 ^{+0.07} _{-0.07}	205 ⁺⁹¹ ₋₈₁
NGC2655	140 ⁺¹⁸⁰ ₋₁₄₀	-	-	-
MRK0704	30 ⁺²³ ₋₂₃	6.29 ^{+0.07} _{-0.09}	0.15 ^{+0.12} _{-0.15}	132 ⁺⁷⁴ ₋₉₁
UGC05101	127 ⁺¹²⁹ ₋₁₂₇	6.55 ^{+0.05} _{-0.04}	< 0.29	170 ⁺⁶⁵⁹ ₋₁₃₅
NGC2992	32 ⁺⁷ ₋₇	6.33 ^{+0.12} _{-0.13}	0.33 ^{+0.35} _{-0.16}	60 ⁺²⁶ ₋₂₄
MESSIER081	38 ⁺¹¹ ₋₁₁	6.6 ^{+0.1} _{-0.1}	< 0.13	23 ⁺²² ₋₁₄
MESSIER082	-	6.48	< 0.01	44
NGC3079	411 ⁺¹⁷³ ₋₁₇₃	6.6 ^{+0.0} _{-0.1}	0.07 ^{+0.19} _{-0.07}	305 ⁺⁹¹⁹ ₋₁₈₃
NGC3147	17 ⁺⁶⁷ ₋₁₇	6.5 ^{+0.1} _{-0.1}	0.05 ^{+0.26} _{-0.05}	162 ⁺³⁹⁴ ₋₁₂₈
NGC3227	174 ⁺²² ₋₂₂	-	-	-
NGC3516	67 ⁺⁸ ₋₈	6.41 ^{+0.02} _{-0.01}	0.12 ^{+0.12} _{-0.92}	132 ⁺¹⁹ ₋₂₂
NGC3690	-	6.6 ^{+0.0} _{-0.1}	0.31 ^{+0.31} _{-0.11}	913 ⁺³⁵⁰ ₋₃₄₆
NGC4051	117 ⁺¹⁹ ₋₁₉	6.55 ^{+0.04} _{-0.15}	0.06 ^{+0.22} _{-0.06}	69 ⁺¹¹⁷ ₋₂₆
NGC4151	174 ⁺¹² ₋₂₀	6.5 ^{+0.0} _{-0.1}	< 0.07	27 ⁺²⁴ ₋₇
NGC4253	45 ⁺⁸ ₋₈	-	-	33 ⁺⁸ ₋₈
NGC4388	144 ⁺²¹ ₋₂₁	-	-	-
MESSIER058	90 ⁺⁴⁴ ₋₄₄	6.6 ^{+0.0} _{-0.1}	0.2 ^{+0.2} _{-0.1}	206 ⁺¹²⁹ ₋₁₀₃
NGC4593	108 ⁺²⁶ ₋₂₆	-	-	-
NGC4631	492 ⁺⁴³¹ ₋₄₇₈	-	-	-
NGC4666	155 ⁺¹⁰⁰ ₋₁₀₀	6.47 ^{+0.04} _{-0.21}	< 0.4	234 ⁺²²⁹ ₋₁₇₀
UGC08058	-	6.49 ^{+0.11} _{-0.13}	0.24 ^{+0.26} _{-0.11}	523 ⁺⁹⁶⁷ ₋₂₃₀
NGC4968	4510 ⁺¹⁶⁹⁷ ₋₁₆₉₇	-	-	-
MCG-03-34-064	139 ⁺²⁹ ₋₂₉	6.2 ^{+0.1} _{-0.0}	0.36 ^{+0.37} _{-0.08}	254 ⁺⁸¹ ₋₈₇
NGC5194	470 ⁺¹⁶⁰ ₋₁₆₀	6.5 ^{+0.1} _{-0.1}	< 0.2	176 ⁺⁷⁹⁵ ₋₁₃₀
ESO383-G035	23 ⁺⁵ ₋₅	6.2 ^{+0.1} _{-0.0}	0.51 ^{+0.5} _{-0.09}	185 ⁺²⁷ ₋₂₆
IRASF13349+2438	-	6.45 ^{+0.15} _{-0.2}	0.61 ^{+0.67} _{-0.13}	774 ⁺²⁵⁹ ₋₂₂₆
NGC5256	362 ⁺²¹⁹ ₋₂₁₉	-	-	-
MRK0273	202 ⁺¹⁰⁵ ₋₁₀₅	-	-	137 ⁺⁹⁵ ₋₉₂
IC4329A	36 ⁺⁴ ₋₄	6.42 ^{+0.08} _{-0.05}	0.3 ^{+0.3} _{-0.1}	72 ⁺¹⁶ ₋₁₃
UGC08850	160 ⁺⁷⁴ ₋₇₄	6.6 ^{+0.0} _{-0.1}	0.06 ^{+0.11} _{-0.06}	132 ⁺⁵⁰⁵ ₋₇₈

Table 9. Continued.

Name	EW _{6.4}	E _{FeKα}	$\sigma_{\text{FeK}\alpha}$	EW _{FeKα}
NGC5506	31 ⁺⁹ ₋₉	6.43 ^{+0.11} _{-0.06}	0.28 ^{+0.33} _{-0.08}	116 ⁺³³ ₋₂₉
NGC5548	22 ⁺⁷ ₋₇	6.4 ^{+0.1} _{-0.1}	0.15 ^{+0.18} _{-0.05}	61 ⁺²⁸ ₋₂₄
2MASXJ15115979	-	6.2 ^{+0.2} _{-0.0}	0.31 ^{+0.46} _{-0.14}	237 ⁺¹⁶⁰ ₋₁₀₆
NGC6240	312 ⁺⁶⁷ ₋₆₇	-	-	134 ⁺⁵⁰ ₋₅₀
NGC6552	1490 ⁺⁵¹⁰ ₋₅₁₀	-	-	-
AM1925-724	194 ⁺²³⁹ ₋₁₉₄	-	-	-
MRK0509	39 ⁺⁷ ₋₇	6.58 ^{+0.02} _{-0.04}	0.00 ^{+0.06} _{-0.01}	17 ⁺⁸ ₋₆
ESO286-IG019	491 ⁺⁷¹⁸ ₋₄₉₁	-	-	-
NGC7172	36 ⁺⁸ ₋₈	6.49 ^{+0.01} _{-0.02}	< 0.01	36 ⁺¹⁰ ₋₈
NGC7213	-	6.39 ^{+0.02} _{-0.02}	0.05 ^{+0.03} _{-0.05}	89 ⁺¹⁸ ₋₁₇
3C445	87 ⁺²⁶ ₋₂₆	-	-	-
NGC7314	16 ⁺⁹ ₋₉	6.46 ^{+0.12} _{-0.1}	0.35 ^{+0.38} _{-0.11}	121 ⁺⁴² ₋₃₅
NGC7469	84 ⁺⁹ ₋₉	-	-	-
NGC7479	768 ⁺⁴²⁹ ₋₄₂₉	-	-	-
NGC7582	370 ⁺²⁹ ₋₂₉	6.6 ^{+0.0} _{-0.1}	0.29 ^{+0.19} _{-0.18}	269 ⁺⁸⁰ ₋₁₇₃
NGC7674	272 ⁺¹⁷³ ₋₁₇₃	-	-	-
NGC7771	-	6.38 ^{+0.22} _{-0.18}	0.18 ^{+0.27} _{-0.18}	487 ⁺⁸⁷⁶ ₋₃₆₅

Table 10. Details of the Compton thick sources found in this sample. Column (1) Galaxy name; Column (2) the directly measured $N_{\text{H}}(\text{cm}^{-2})$; Column (3) the EW of the Fe K α line (eV); Column (4) the reflection fraction determined from the `pxmon` model.

Name (1)	$\log_{10}(N_{\text{H}})$ (2)	EW (3)	R (4)
NGC1068	-	677	10.3
NGC1320	24.3 ^{+1.2} _{-0.3}	940 ⁺⁸⁵¹ ₋₅₈₅	40.4 ^{+44.9} ₋₃₉
NGC1386	20.7 ^{+0.1} _{-0.1}	1710 ⁺³⁷³ ₋₃₇₃	145 ⁺¹⁶⁰ ₋₁₄₇
NGC1667	24.4 ^{+1.8} _{-1.1}	-	-
NGC3079	20.7 ^{+0.3} _{-0.7}	716 ⁺²¹⁸⁰ ₋₅₂₅	16.3 ^{+7.84} _{-9.7}
NGC3690	20.8 ^{+0.3} _{-0.8}	913 ⁺³⁸⁰ ₋₃₄₆	-
MESSIER088	21.3 ^{+0.4} _{-0.2}	-	17.6 ^{+24.2} _{-17.6}
NGC4968	24.5 ^{+0.9} _{-0.3}	4510 ⁺¹⁷⁰⁰ ₋₁₇₀₀	-
NGC5194	20.6 ^{+0.1} _{-0.1}	646 ⁺²⁹³⁰ ₋₅₂₅	51.3 ^{+31.6} _{-41.1}
2MASXJ15504152	21.6 ^{+0.4} _{-0.7}	-	13.7 ^{+59.5} _{-8.87}
NGC6552	-	1490 ⁺⁵¹⁰ ₋₅₁₀	112 ^{+83.2} _{-47.7}
NGC6890	21.0 ^{+0.5} _{-0.7}	-	52.1 ^{+43.2} ₋₄₇
NGC7479	24.3 ^{+0.5} _{-0.4}	768 ⁺⁴²⁹ ₋₄₂₉	0.29 ^{+3.71} _{-0.3}
ESO148-IG002	-	-	41.6 ^{+32.6} _{-43.1}
NGC7582	20.6	639 ⁺¹⁹⁷ ₋₄₁₄	107
NGC7674	-	272 ⁺¹⁷³ ₋₁₇₃	143 ⁺¹²⁰ ₋₁₄₈